Design of a Nonhydrostatic Atmospheric Model Based on a Generalized Vertical Coordinate

MICHAEL D. TOY AND DAVID A. RANDALL

Department of Atmospheric Science, Colorado State University, Fort Collins, Colorado

(Manuscript received 23 October 2008, in final form 30 December 2008)

ABSTRACT

The isentropic system of equations has particular advantages in the numerical modeling of weather and climate. These include the elimination of the vertical velocity in adiabatic flow, which simplifies the motion to a two-dimensional problem and greatly reduces the numerical errors associated with vertical advection. The mechanism for the vertical transfer of horizontal momentum is simply the pressure drag acting on isentropic coordinate surfaces under frictionless, adiabatic conditions. In addition, vertical resolution is enhanced in regions of high static stability, which leads to better resolution of features such as the tropopause. Negative static stability and isentropic overturning frequently occur in finescale atmospheric motion. This presents a challenge to nonhydrostatic modeling with the isentropic vertical coordinate. This paper presents a new nonhydrostatic atmospheric model based on a generalized vertical coordinate. The coordinate is specified in a manner similar to that of Konor and Arakawa, but ''arbitrary Eulerian–Lagrangian'' (ALE) methods are used to maintain coordinate monotonicity in regions of negative static stability and to return the coordinate surfaces to their isentropic ''targets'' in statically stable regions. The model is mass conserving and implements a vertical differencing scheme that satisfies two additional integral constraints for the limiting case of z coordinates. The hybrid vertical coordinate model is tested with mountain-wave experiments including a downslope windstorm with breaking gravity waves. The results show that the advantages of the isentropic coordinate are realized in the model with regard to vertical tracer and momentum transport. Also, the isentropic overturning associated with the wave breaking is successfully handled by the coordinate formulation.

1. Introduction

Since the introduction of the quasi-Lagrangian system of equations by Starr (1945), potential temperature (θ) has gradually become more widely used as a vertical coordinate in numerical atmospheric models. The primary advantage of the θ coordinate is that the vertical velocity $\dot{\theta} \equiv D\theta/Dt$ is zero for adiabatic processes, which reduces the numerical error associated with vertical advection. However, difficulties include negative static stability, produced, for example, by the overturning of isentropic surfaces and planetary boundary layer (PBL) processes, and the intersection of isentropic surfaces with the lower boundary. The latter issue has been overcome in the successful development of various quasi-static θ-coordinate models (e.g., Eliassen and Raustein 1968; Bleck 1984; Hsu and Arakawa 1990). Hybrid vertical coordinates have been developed to address the issues of lower-boundary coordinate intersection and the lack of vertical resolution in the PBL. With this method, a terrain-following (σ) coordinate is used in the lowest model layers, while the free atmosphere is represented by θ coordinates. Quasi-static models using hybrid coordinates include Uccellini et al. (1979), Zhu et al. (1992), Bleck and Benjamin (1993), Johnson et al. (1993), Konor and Arakawa (1997), Benjamin et al. (2004), Schaack et al. (2004), and Dowling et al. (2006).

With advances in computer technology, large-domain weather forecasting and global climate models are being developed with high horizontal resolution ($\Delta x \lesssim 10$ km) and nonhydrostatic dynamical cores that resolve finescale atmospheric motions (e.g., Skamarock et al. 2005; Davies et al. 2005; Satoh et al. 2008). On these scales, isentropic overturning associated with wave breaking and convection is a common feature. Because of this, using θ coordinates in nonhydrostatic models is a challenge.

Corresponding author address: Dr. Michael D. Toy, Dept. of Atmospheric Science, Colorado State University, Fort Collins, CO 80523.
E-mail: toy@atmos.colostate.edu

DOI: 10.1175/2009MWR2834.1

Only in the past decade have nonhydrostatic hybrid (θ–σ) coordinate models been developed (e.g., Skamarock 1998; He 2002; Zängl 2007).

Skamarock (1998) and He (2002) extended the hybrid coordinate method of Bleck and Benjamin (1993) to the nonhydrostatic system. Their methods involve a regridding algorithm in which minimum and maximum layer-thickness requirements are imposed in order to provide vertical resolution in statically unstable regions, that is, where $\partial\theta/\partial z < 0$. Under regridding, mass is vertically exchanged to maintain layer separation. Spatial smoothing is applied to coordinate surfaces, which helps maintain layer separation and prevent surfaces from becoming vertical. Successful two-dimensional mountain wave-breaking experiments were achieved by both Skamarock (1998) and He (2002). With the latter model, a three-dimensional simulation of baroclinic wave growth on a β plane was also performed.

Zängl (2007) developed a version of the nonhydrostatic Weather Research and Forecasting Model (WRF; Skamarock et al. 2005) that uses an adaptive vertical grid. The value of the terrain-following hydrostatic-pressure vertical coordinate (Laprise 1992), used in the WRF model, is calculated at each grid point using a prognostic equation. This is a relaxation–diffusion equation that nudges the coordinate toward a "target" field. The specification of the target field determines the nature of the coordinate. Zängl specified the target field to be terrain following near the surface and isentropic in the free atmosphere. A diffusion term in the prognostic equation maintains an even layer spacing, smoothness in the horizontal, and coordinate monotonicity in regions of isentropic overturning.

The designs of the vertical coordinate in these nonhydrostatic models were influenced by arbitrary Lagrangian–Eulerian (ALE) methods (Hirt et al. 1974) and adaptive grid techniques (Dietachmayer and Droegemeier 1992). With the ALE method, the three-dimensional spatial arrangement of the model grid is predicted in a Lagrangian manner. However, mass is allowed to cross grid-cell walls, as necessary, to maintain grid regularity. In contrast, the hybrid coordinate method of Konor and Arakawa (1997, hereafter KA97) is not derivative of ALE or adaptive grid techniques. In their model, the vertical coordinate is a specified function of θ and σ, with a smooth transition with height toward isentropic coordinates. As a result, the combination of the quasi-Lagrangian (θ) and Eulerian (σ) components is strictly prescribed at each model level.

In this paper, we describe a new nonhydrostatic, hybrid vertical coordinate atmospheric model based on the vertical coordinate of KA97, but incorporating the adaptive grid methods similar to those of the earlier nonhydrostatic hybrid-coordinate models mentioned above. Section 2 of this paper describes the continuous system of equations based on a generalized vertical coordinate, the specification of the vertical coordinate, and the diagnosis of the generalized vertical velocity. The methods used to smooth the grid are introduced within the context of the continuous system. In section 3, the vertical grid and the vertically discrete system of equations are presented. Simulations of 2D mountain waves are presented in section 4. These include an idealized small-amplitude case, and a large-amplitude case based on the 11 January 1972 Boulder, Colorado, windstorm. A summary and conclusions are presented in section 5.

2. The continuous system of equations

Our model is based on the compressible nonhydrostatic Eulerian equations of fluid motion in a generalized vertical coordinate. These are the primitive equations reviewed in Kasahara (1974), but with the vertical acceleration term, Dw/Dt, restored in the vertical momentum equation. In this section, we present the governing equations used in the model. The vertical coordinate is then presented, along with the method for diagnosing the generalized vertical velocity. Finally, we will analyze the vertical flux of horizontal momentum in the generalized vertical coordinate. The resulting expressions will be used to contrast the fluxes in the model with Eulerian versus quasi-Lagrangian vertical coordinates.

a. Governing equations

The material time derivative expressed in the generalized vertical coordinate η is written as

$$\frac{D}{Dt} = \frac{\partial}{\partial t} + \mathbf{v}\cdot\nabla + \dot{\eta}\frac{\partial}{\partial \eta}, \tag{2.1}$$

where the partial time derivative and the horizontal-gradient operator ∇ are evaluated on constant-η surfaces, $\dot{\eta} \equiv D\eta/Dt$ is the generalized vertical velocity, and $\mathbf{v}$ is the horizontal velocity.

The mass continuity equation is expressed in terms of the pseudodensity m as

$$\frac{\partial m}{\partial t} + \nabla\cdot(m\mathbf{v}) + \frac{\partial}{\partial \eta}(m\dot{\eta}) = 0, \tag{2.2}$$

where

$$m \equiv \rho\frac{\partial z}{\partial \eta}. \tag{2.3}$$

Here, ρ is density and z is geopotential height. The upper and lower boundaries are assumed to be material, constant-η surfaces, so the boundary conditions are

$$(m\dot{\eta})_T = (m\dot{\eta})_S = 0, \tag{2.4}$$

where the subscripts T and S refer to the upper and lower boundaries, respectively. The horizontal momentum equation is given by

$$\frac{D\mathbf{v}}{Dt} + f\mathbf{k} \times \mathbf{v} = \mathbf{HPGF} + \mathbf{F}, \tag{2.5}$$

where f is the Coriolis parameter, $\mathbf{k}$ is the vertical unit vector, **HPGF** is the horizontal pressure-gradient force vector, and **F** is the horizontal friction force. The horizontal pressure-gradient force may be written in terms of pressure (p) as

$$\mathbf{HPGF} = -\frac{1}{\rho}\nabla_\eta p + \frac{1}{mg}\frac{\partial p}{\partial \eta}\nabla_\eta \phi, \tag{2.6a}$$

or in terms of the Exner function (Π) as

$$\mathbf{HPGF} = -\theta\nabla_\eta \Pi + \theta\frac{\partial \Pi}{\partial \phi}\nabla_\eta \phi, \tag{2.6b}$$

where g is gravity, $\phi = gz$ is the geopotential, the Exner function is defined by

$$\Pi \equiv c_p\left(\frac{p}{p_0}\right)^\kappa, \tag{2.7}$$

and θ is the potential temperature given by

$$\theta = \frac{c_p T}{\Pi}, \tag{2.8}$$

where T is temperature. The vertical momentum equation is

$$\frac{Dw}{Dt} = \mathrm{VPGF} - g + F_z, \tag{2.9}$$

where w is the vertical velocity, VPGF is the vertical pressure-gradient force, and F_z is the vertical component of the friction force. The vertical pressure-gradient force may be written in terms of pressure as

$$\mathrm{VPGF} = -\frac{1}{m}\frac{\partial p}{\partial \eta}, \tag{2.10a}$$

or in terms of the Exner function as

$$\mathrm{VPGF} = -g\theta\frac{\partial \Pi}{\partial \phi}. \tag{2.10b}$$

The lower boundary condition on w is given by

$$w_S = \mathbf{v}_S \cdot \nabla z_S. \tag{2.11}$$

The thermodynamic energy equation can be written in terms of the potential temperature as

$$\frac{\partial \theta}{\partial t} + \mathbf{v}\cdot\nabla\theta + \dot{\eta}\frac{\partial \theta}{\partial \eta} = \frac{Q}{\Pi}, \tag{2.12}$$

where Q is the diabatic heating. Within the generalized vertical coordinate framework, geopotential height is a dependent variable. Using the definition $w \equiv Dz/Dt$, we can write the tendency equation for z as

$$\frac{\partial z}{\partial t} + \mathbf{v}\cdot\nabla z + \dot{\eta}\frac{\partial z}{\partial \eta} = w. \tag{2.13}$$

The atmosphere is assumed to be an ideal gas for which the equation of state is given by

$$p = \rho RT, \tag{2.14}$$

where R is the gas constant for dry air.

We define a terrain-following, height-based vertical coordinate σ as

$$\sigma \equiv \frac{z - z_S}{z_T - z_S}, \tag{2.15}$$

which is a variant of the coordinate introduced by Gal-Chen and Somerville (1975).

Neglecting diabatic heating and frictional forces, the set of equations given by (2.2)–(2.15) is one equation short of being a closed system. The remaining relation to be specified is that for the dependent variable $\dot{\eta}$, the generalized vertical velocity, which is discussed in the following subsection.

b. Specification of the vertical coordinate and diagnosis of the generalized vertical velocity

1) THE VERTICAL COORDINATE

The above system of governing equations can be closed by specifying the vertical coordinate as a function of any combination of the dependent variables, as long as that function is monotonic in height. This leads to the determination of the generalized vertical velocity $\dot{\eta}$. For example, choosing $\eta = z$ leads to $\dot{\eta} = \dot{z} = w$, while choosing $\eta = \theta$ leads to $\dot{\eta} = \dot{\theta} = Q/\Pi$. We employ an alternative approach, which is to reverse this process by specifying the generalized vertical velocity, and apply it in the vertical advection terms of the prognostic equations. As a result, η is not necessarily defined in terms of the dependent variables, yet it still serves as the vertical coordinate as long as it remains monotonic in height. This condition is met as long as the height field, determined by (2.13), remains a monotonic function of η. If

this condition is violated, then the generalized vertical velocity may be respecified to maintain monotonicity. This approach is reminiscent of the ALE method of Hirt et al. (1974). Within the ALE framework, the generalized vertical velocity would be specified as zero until the height field becomes nonmonotonic, at which point an adjustment would be made. Lin (2004) employs a similar method.

As a further example of the approach described above, if η were initially specified as the quasi-Lagrangian isentropic coordinate, then choosing $\dot{\eta} = Q/\Pi$ would automatically satisfy $\partial\theta/\partial t = 0$ through (2.12), which maintains $\theta = \eta$. Similarly, if η were initially specified to be the geopotential height, then choosing $\dot{\eta} = w$ would satisfy $\partial z/\partial t = 0$ through (2.13), maintaining $z = \eta$. In the first example, the vertical coordinate is the "target value" for the potential temperature, while in the latter, it is the target value for the height.

The vertical coordinate in our model is based on the hybrid σ–θ coordinate developed by KA97. It is the terrain-following σ coordinate near the surface and transitions to θ coordinates with height. The coordinate serves as a target field for a specified function $F(\theta, \sigma)$. Therefore, the generalized vertical velocity diagnosis primarily follows KA97, but is modified in order to maintain coordinate monotonicity as well as specific requirements on the spatial distribution, or "smoothness," of coordinate isosurfaces, to be described below. The maintenance of monotonicity near the surface is provided by the σ contribution to the vertical coordinate, while in the free atmosphere, where the coordinate is primarily θ, monotonicity is maintained by an adaptive grid method (e.g., Skamarock 1998; He 2002; Zängl 2007). While this method is typically associated with the discrete grid framework, here we formulate it in the continuous system.

The target relationship for the variables θ and σ is

$$F(\theta, \sigma) = f(\sigma) + g(\sigma)\theta, \tag{2.16}$$

where the functions $f(\sigma)$ and $g(\sigma)$ are chosen such that

$$\left.\begin{array}{lll} g(\sigma) \to 0; & & \sigma \to \sigma_S \\ f(\sigma) \to 0, & g(\sigma) \to 1; & \sigma \to \sigma_T \end{array}\right\}. \tag{2.17}$$

The form of $g(\sigma)$ that we use in the model is

$$g(\sigma) = 1 - (1 - \sigma)^r, \tag{2.18}$$

where r is a constant greater than unity. This choice satisfies (2.17), and the thickness of the σ-like domain near the surface can be controlled by the value of r: the larger its value, the nearer the surface the coordinate becomes fully isentropic. In KA97, the requirement $\partial F/\partial\eta > 0$ is satisfied by choosing $f(\sigma)$ from

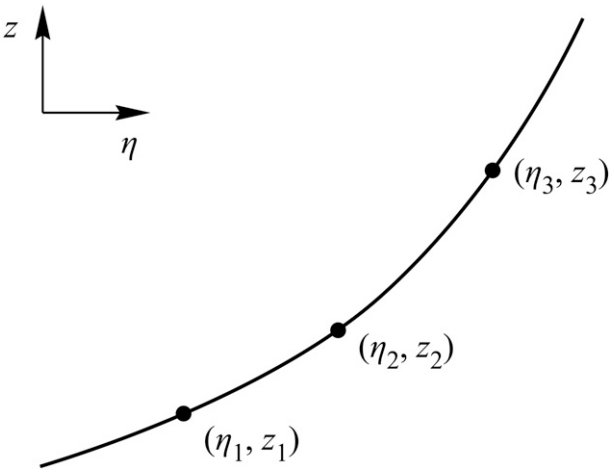

FIG. 1. Three discrete points along a continuous profile of z as a function of η. Used to derive the mathematical form of the "vertical smoothness parameter."

$$\frac{df}{d\sigma} + \frac{dg}{d\sigma}\theta_{\min} + g\left(\frac{\partial\theta}{\partial\sigma}\right)_{\min} = 0, \tag{2.19}$$

where $\theta_{\min}$ and $(\partial\theta/\partial\sigma)_{\min}$ are suitably chosen parameters representing the lower bounds of the potential temperature and static stability, respectively. In the model, we specify $(\partial\theta/\partial\sigma)_{\min} = 0$. This means that the condition $\partial F/\partial\eta > 0$ is not necessarily met for statically unstable profiles. However, unlike KA97, in which $\eta \equiv F$, we allow F to depart from its time-independent target value η in order to maintain the requirement $\partial\eta/\partial\sigma > 0$, as shown below.

The time tendency of F is given by

$$\left(\frac{\partial}{\partial t}\right)_{\eta} F(\theta, \sigma) = \frac{\eta - F(\theta, \sigma)}{\tau_{\text{rel}}} - \dot{\eta}_S \frac{\partial F}{\partial \eta}, \tag{2.20}$$

where τ_{rel} is a relaxation time constant, and $\dot{\eta}_S$ is the smoothing contribution to the generalized vertical velocity to be described below. The first term on the rhs of (2.20) is a Newtonian relaxation term that relaxes F toward its target value η. The second term is an advective adjustment to F required to satisfy two smoothness criteria for coordinate isosurfaces, as described below. Note that in KA97, for which $\eta = F$ by definition, the rhs of (2.20) is identically zero.

We prescribe two smoothness criteria for the spatial arrangement of coordinate isosurfaces: a horizontal criterion to maintain

$$\left|\nabla^4 z\right| < (\nabla^4 z)_{\max}, \tag{2.21}$$

and a vertical criterion to maintain

$$\left|\frac{\dfrac{\partial^2 z}{\partial \eta^2}}{\dfrac{\partial z}{\partial \eta}}\right| < \left(\frac{\dfrac{\partial^2 z}{\partial \eta^2}}{\dfrac{\partial z}{\partial \eta}}\right)_{\max}, \tag{2.22}$$

where the $()_{\max}$ values in the above equations are specified maximum limits. The horizontal criterion (2.21) is designed to limit the existence of sharp horizontal gradients and their associated truncation errors in the discrete model. The vertical criterion (2.22) eliminates the possibility of η from becoming nonmonotonic with height, and in the discrete model, it prevents the relative difference in the thickness of adjacent layers from becoming too large. It basically serves to keep the distribution of layer thicknesses in a model column evenly distributed. This can be seen by considering a representative continuous relationship between z and η, as shown in Fig. 1. Three points are shown along the curve that represent discrete model positions. The relative difference in the thickness of adjacent layers is expressed by the nondimensional parameter

$$\frac{\delta^2 z}{\delta z} \equiv \frac{(z_3 - z_2) - (z_2 - z_1)}{\dfrac{1}{2}(z_3 - z_1)}, \tag{2.23}$$

where the δ^2 operator refers to the difference operator δ recursively applied twice. Applying a Taylor series expansion to (2.23), we obtain

$$\frac{\delta^2 z}{\delta z} = \frac{\dfrac{1}{2}\left(\dfrac{\partial^2 z}{\partial \eta^2}\right)_2 [(\delta\eta)_B^2 + (\delta\eta)_A^2] + \left(\dfrac{\partial z}{\partial \eta}\right)_2 [(\delta\eta)_B - (\delta\eta)_A] + \cdots}{\left(\dfrac{\partial z}{\partial \eta}\right)_2 \dfrac{1}{2}[(\delta\eta)_B + (\delta\eta)_A] + \dfrac{1}{4}\left(\dfrac{\partial^2 z}{\partial \eta^2}\right)_2 [(\delta\eta)_B^2 - (\delta\eta)_A^2] + \cdots}, \tag{2.24}$$

where the subscript "2" denotes continuous derivatives at the discrete point "2", $(\delta\eta)_A \equiv \eta_2 - \eta_1$, and $(\delta\eta)_B \equiv \eta_3 - \eta_2$. For $(\delta\eta)_A = (\delta\eta)_B = (\delta\eta)$, and truncating the Taylor series, we have

$$\frac{\delta^2 z}{\delta z} \cong \frac{\left(\dfrac{\partial^2 z}{\partial \eta^2}\right)}{\left(\dfrac{\partial z}{\partial \eta}\right)} (\delta\eta), \tag{2.25}$$

which is the basis of the vertical smoothness parameter in (2.22).

In short, the formulation of the vertical coordinate involves two groups of "tunable" coefficients: 1) the KA97 parameters r, $\theta_{\min}$, and $(\partial\theta/\partial\sigma)_{\min}$; and 2) the smoothness parameters associated with the adaptive grid method. Optimal values for these mainly depend on the spatial scales of the atmospheric phenomena under investigation (which drive the choice of the smoothness parameters), the height above the surface above which the coordinate becomes isentropic, the time scale to return to the target value of $F(\theta, \sigma)$, and the expected lower bound for the potential temperature in the domain. So far we have tested the model in limited-area case studies, and it provides good results for a wide range of parameter values. However, when the model is extended to the global domain, the optimal values will vary in space and time. It may then be desirable to add the flexibility of having the parameters vary in order to optimally represent the various atmospheric regimes encountered globally and seasonally.

2) DIAGNOSIS OF THE GENERALIZED VERTICAL VELOCITY

Equation (2.20) serves as the starting point for the diagnosis of the generalized vertical velocity. Note that when the rhs of (2.20) is zero, the vertical velocity has the same form as in KA97. For convenience, we express the generalized vertical velocity as the sum of two contributions; that is,

$$\dot{\eta} = \dot{\eta}_T + \dot{\eta}_S, \tag{2.26}$$

where $\dot{\eta}_T$ is the "target seeking" contribution that maintains $F(\theta, \sigma)$ at (or relaxes it toward) its target value η and $\dot{\eta}_S$ is the smoothing contribution, introduced in (2.20), which provides the advective adjustment needed to maintain the spatial smoothness of the coordinate isosurfaces.

(i) "Target seeking" contribution to the generalized vertical velocity

Considering $\dot{\eta}_S$ equal to zero in (2.20), and applying the chain rule of differentiation to the lhs of (2.20), we can write

$$\left(\frac{\partial F}{\partial \theta}\right)_\sigma \frac{\partial \theta}{\partial t} + \left(\frac{\partial F}{\partial \sigma}\right)_\theta \frac{\partial \sigma}{\partial t} = \frac{\eta - F(\theta, \sigma)}{\tau_{\text{rel}}}. \tag{2.27}$$

Combining (2.12), (2.13), (2.15), and (2.27), and solving for the generalized vertical velocity, we obtain

$$\dot{\eta}_T = \left(\frac{\partial F}{\partial \eta}\right)^{-1}\left[\left(\frac{\partial F}{\partial \theta}\right)_\sigma\left(\frac{Q}{\Pi} - \mathbf{v}\cdot\nabla\theta\right) + \left(\frac{\partial F}{\partial \sigma}\right)_\theta \frac{1}{H}(w - \mathbf{v}\cdot\nabla z) + \frac{F(\theta,\sigma) - \eta}{\tau_{\rm rel}}\right], \quad (2.28)$$

where

$$H \equiv z_T - z_S, \quad (2.29)$$

which is the column height, and we used

$$\frac{\partial F}{\partial \eta} = \frac{\partial \theta}{\partial \eta}\left(\frac{\partial F}{\partial \theta}\right)_\sigma + \frac{1}{H}\frac{\partial z}{\partial \eta}\left(\frac{\partial F}{\partial \sigma}\right)_\theta. \quad (2.30)$$

For $F = \eta$, (2.28) expresses the generalized vertical velocity of KA97. When $F \neq \eta$, (2.28) has a singularity for $\partial F/\partial\eta = 0$, which occurs in neutrally stable environments and $F \approx \theta$. Therefore, we must modify the generalized vertical velocity to avoid this singularity. A straightforward method is to "freeze" the coordinate isolines in space, such that $\partial z/\partial t = 0$, as $\partial F/\partial\eta$ approaches zero, as well as for $\partial F/\partial\eta < 0$. In other words, the coordinate becomes a stationary, Eulerian coordinate in regions of negative static stability. From (2.13), we then write

$$\dot{\eta}_T = \left(\frac{\partial z}{\partial \eta}\right)^{-1}(w - \mathbf{v}\cdot\nabla z) \quad \text{for} \quad \frac{\partial F}{\partial \eta} \le 0. \quad (2.31)$$

For $\partial F/\partial\eta \ge \beta$, we use (2.28), where β is a parameter with a value between 0 and 1. For $0 < \partial F/\partial\eta < \beta$, we use a linear combination of (2.31) and (2.28) evaluated with $\partial F/\partial\eta = \beta$; that is,

$$\dot{\eta}_T = \left(1 - \frac{1}{\beta}\frac{\partial F}{\partial \eta}\right)[\text{rhs eqn. (2.31)}] + \frac{1}{\beta}\frac{\partial F}{\partial \eta}\left[\text{rhs eqn. (2.28)} \quad \text{with} \quad \frac{\partial F}{\partial \eta} = \beta\right] \quad \text{for} \quad 0 < \frac{\partial F}{\partial \eta} < \beta. \quad (2.32)$$

The result is

$$\dot{\eta}_T = \left(1 - \frac{1}{\beta}\frac{\partial F}{\partial \eta}\right)\left(\frac{\partial z}{\partial \eta}\right)^{-1}(w - \mathbf{v}\cdot\nabla z) + \frac{1}{\beta^2}\frac{\partial F}{\partial \eta}\left[\left(\frac{\partial F}{\partial \theta}\right)_\sigma\left(\frac{Q}{\Pi} - \mathbf{v}\cdot\nabla\theta\right) + \left(\frac{\partial F}{\partial \sigma}\right)_\theta \frac{1}{H}(w - \mathbf{v}\cdot\nabla z) + \frac{F(\theta,\sigma) - \eta}{\tau_{\rm rel}}\right] \quad \text{for} \quad 0 < \frac{\partial F}{\partial \eta} < \beta. \quad (2.33)$$

(ii) Smoothing contribution to the generalized vertical velocity

The generalized vertical velocity contribution required to advectively adjust the geopotential height field, per the horizontal and vertical smoothness criteria described above, is calculated from

$$\dot{\eta}_S = -\left[\left(\frac{\partial z}{\partial t}\right)_{\substack{\text{smoothing,}\\ \text{horiz}}} + \left(\frac{\partial z}{\partial t}\right)_{\substack{\text{smoothing,}\\ \text{vert}}}\right]\frac{\partial \eta}{\partial z}, \quad (2.34)$$

where the two terms in brackets are the height tendencies due to horizontal and vertical smoothing.

The horizontal smoothing tendency is quantified in the form of a "del-4" diffusion equation given by

$$\left(\frac{\partial z}{\partial t}\right)_{\substack{\text{smoothing,}\\ \text{horiz}}} = -(\max\{0, \kappa_{\rm horiz}[|\nabla^4 z| - (\nabla^4 z)_{\rm max}]\}\text{sgn}(\nabla^4 z)), \quad (2.35)$$

where $\kappa_{\rm horiz}$ is a constant diffusion coefficient. The smoothing tendency is nonzero only when $|\nabla^4 z| > (\nabla^4 z)_{\rm max}$. The vertical smoothing tendency is similarly expressed using second-order diffusion. The vertical smoothing tendency is given by

$$\left(\frac{\partial z}{\partial t}\right)_{\substack{\text{smoothing,}\\ \text{vert}}} = \max\left\{0, \kappa_{\rm vert}\left[\left|\frac{\partial^2 z}{\partial \eta^2}\right| - \frac{\partial z}{\partial \eta}\left(\frac{\dfrac{\partial^2 z}{\partial \eta^2}}{\dfrac{\partial z}{\partial \eta}}\right)_{\rm max}\right]\right\}\text{sgn}\left(\frac{\partial^2 z}{\partial \eta^2}\right), \quad (2.36)$$

where κ_{vert} is a constant diffusion coefficient. Vertical diffusion only acts when the absolute value of the ratio of the second and first derivatives of z with respect to η exceeds the specified limit.

c. *Vertical flux of horizontal momentum in a generalized vertical coordinate*

In this section we derive a time tendency equation for the zonally averaged zonal velocity for the purpose of diagnosing the vertical momentum flux in the model. This is done to test the model's accuracy and to contrast the form of the fluxes within the σ- and hybrid-vertical coordinate frameworks. In the derivation, we determine an expression for the Eliassen–Palm (EP) flux in a generalized vertical coordinate. The derivation follows Andrews (1983), who derived the EP flux in isentropic coordinates for quasi-static flow.

Combining (2.1), (2.3), (2.5), and (2.6a), the zonal momentum equation can be written

$$\frac{\partial u}{\partial t} + u\frac{\partial u}{\partial x} + v\frac{\partial u}{\partial y} + \dot{\eta}\frac{\partial u}{\partial \eta} - fv = \frac{1}{m}\left[-\frac{\partial}{\partial x}\left(p\frac{\partial z}{\partial \eta}\right) + \frac{\partial}{\partial \eta}\left(p\frac{\partial z}{\partial x}\right)\right] + F_x, \tag{2.37}$$

where u and v are the zonal and meridional velocity components, respectively, and F_x is the zonal component of the friction force. Combining (2.37) with the continuity equation (2.2), the zonal momentum equation in flux form can be written as

$$\frac{\partial}{\partial t}(mu) + \frac{\partial}{\partial x}(muu) + \frac{\partial}{\partial y}(muv) + \frac{\partial}{\partial \eta}(mu\dot{\eta}) - fmv = -\frac{\partial}{\partial x}\left(p\frac{\partial z}{\partial \eta}\right) + \frac{\partial}{\partial \eta}\left(p\frac{\partial z}{\partial x}\right) + mF_x. \tag{2.38}$$

The zonal average of a given property a may be defined as

$$\overline{a} \equiv \frac{1}{L}\int_{-L/2}^{L/2} a\,dx, \tag{2.39}$$

where L is the length of the domain in the zonal direction. Applying (2.39) to (2.38), we obtain

$$\frac{\partial}{\partial t}(\overline{mu}) + \frac{\partial}{\partial y}(\overline{muv}) + \frac{\partial}{\partial \eta}(\overline{mu\dot{\eta}}) - f\overline{mv} = \frac{\partial}{\partial \eta}\left(\overline{p\frac{\partial z}{\partial x}}\right) + \overline{mF_x}, \tag{2.40}$$

where we used

$$\overline{\frac{\partial}{\partial x}(\ )} = 0. \tag{2.41}$$

In a similar manner, the zonally averaged continuity Eq. (2.2) is

$$\frac{\partial}{\partial t}\overline{m} + \frac{\partial}{\partial y}(\overline{mv}) + \frac{\partial}{\partial \eta}(\overline{m\dot{\eta}}) = 0. \tag{2.42}$$

Now divide the fluid properties into mean and perturbation components so that

$$a = \overline{a} + a', \tag{2.43}$$

where the prime notation represents perturbations from the mean. Under Reynolds averaging, we have

$$\overline{a'} = 0 \tag{2.44}$$

and

$$\overline{ma} = \overline{m}\,\overline{a} + \overline{m'a'}. \tag{2.45}$$

Combining (2.40) and (2.42), and applying (2.45), we can write the zonally averaged zonal momentum tendency equation as

$$\frac{\partial}{\partial t}\overline{u} + \frac{\overline{mv}}{\overline{m}}\left(\frac{\partial}{\partial y}\overline{u} - f\right) + \frac{\overline{m\dot{\eta}}}{\overline{m}}\frac{\partial}{\partial \eta}\overline{u} = \frac{1}{\overline{m}}\left\{-\frac{\partial}{\partial y}\overline{(mv)'u'} + \frac{\partial}{\partial \eta}\left[\overline{p'\frac{\partial z'}{\partial x}} - \overline{(m\dot{\eta})'u'}\right] - \frac{\partial}{\partial t}(\overline{m'u'})\right\} + \frac{\overline{mF_x}}{\overline{m}}. \tag{2.46}$$

Following Andrews (1983), the mass-weighted "residual" mean velocities are defined as

$$\overline{v}^* \equiv \frac{\overline{mv}}{\overline{m}} \tag{2.47}$$

and

$$\overline{\dot{\eta}}^* \equiv \frac{\overline{m\dot{\eta}}}{\overline{m}}. \tag{2.48}$$

Applying (2.47) and (2.48) in (2.46), we obtain

$$\frac{\partial}{\partial t}\overline{u} + \overline{v}^*\left(\frac{\partial}{\partial y}\overline{u} - f\right) + \overline{\dot{\eta}}^*\frac{\partial}{\partial \eta}\overline{u} = \frac{1}{\overline{m}}\left[\nabla^{(\eta)}\cdot\mathbf{F}^{(\eta)} - \frac{\partial}{\partial t}(\overline{m'u'})\right] + \frac{\overline{mF_x}}{\overline{m}}, \tag{2.49}$$

where $\mathbf{F}^{(\eta)} \equiv [0, F_y^{(\eta)}, F_\eta^{(\eta)}]$ is the EP flux vector in generalized vertical coordinates, which has the meridional and vertical components

$$F_y^{(\eta)} = \overline{(mv)'u'} \tag{2.50}$$

and

$$F_\eta^{(\eta)} = \overline{p' \frac{\partial z'}{\partial x}} - \overline{(m\dot{\eta})'u'}, \tag{2.51}$$

respectively. Equation (2.49) shows that the EP flux is nondivergent for steady-state, uniform, frictionless flow.

The vertical component of the EP flux given by (2.51) is the vertical flux of the horizontal momentum. In z coordinates, the first term on the rhs is zero, which leaves the eddy flux term $-\overline{(\rho w)'u'}$ as the means of vertical momentum transport. In θ coordinates, for adiabatic conditions, $\dot{\eta}' = \dot{\theta}' = 0$, which means the vertical momentum transport occurs through the first term on the rhs of (2.51), that is, the pressure form drag on coordinate (material) surfaces. This is consistent with the fact that the zonal average of the "mountain torque" term in [(A.1), see the appendix], which is the pressure form drag on the lower (material) boundary, represents the momentum flux across the earth's surface. Klemp and Lilly (1978) also noted the equivalence of the pressure drag and momentum flux in isentropic coordinates.

3. Vertical discretization

The vertically discrete governing equations presented in this section form the basis of the scheme used in the model. Centered vertical differences are shown in the analysis, although upstream-weighted advection schemes (Takacs 1985) for mass and potential temperature are actually used in the model. Details of these schemes can be found in Toy (2008).

a. Vertical grid

The vertical staggering of the prognostic variables of the model, shown in Fig. 2, is based on the Charney–Phillips (CP) grid (Charney and Phillips 1953) developed for hydrostatic p-based coordinate models. This grid is also the basis of the generalized vertical coordinate model of KA97. With the CP grid, the potential temperature is staggered with respect to the horizontal velocity. Another commonly used staggering is the Lorenz (L) grid (Lorenz 1960) in which the potential temperature is carried at the same levels as the horizontal velocity. The advantages of the CP grid over the L grid in quasi-static modeling have been analyzed in various papers (e.g., Arakawa and Moorthi 1988; Arakawa and Konor 1996). Thuburn and Woollings (2005), Toy and Randall (2007), and Toy (2008) have pointed out similar advantages to the CP grid in nonhydrostatic z-based coordinate models. These include the avoidance of vertical computational modes as well as improved accuracy in the representation of vertical wave propagation.

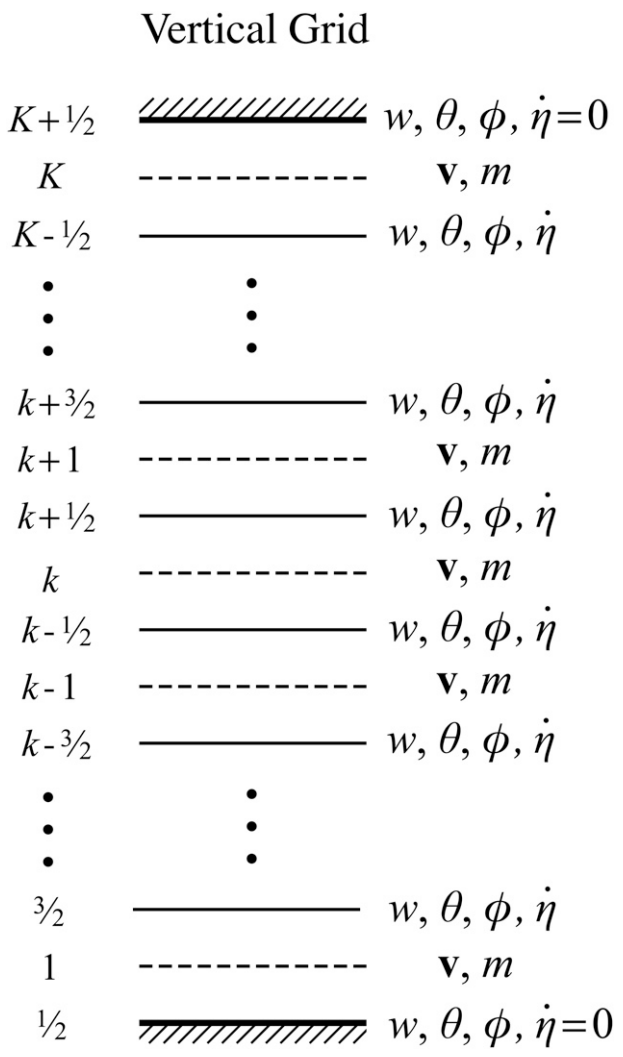

FIG. 2. Vertical grid used in the model.

The grid indexing used in the vertical discretization is shown in Fig. 2. There are K layers in the model numbered from bottom to top. Layer centers are numbered by whole integers, k, and layer edges by half-integers.

b. Continuity equation

The discretized form of the continuity Eq. (2.2) is given by

$$\frac{\partial m_k}{\partial t} + \nabla \cdot (m\mathbf{v})_k + \frac{(m\dot{\eta})_{k+1/2} - (m\dot{\eta})_{k-1/2}}{(\delta\eta)_k} = 0 \quad \text{for } k = 1, 2, \cdots, K, \tag{3.1}$$

where the difference operator δ is defined as $(\delta\, a)_k \equiv a_{k+1/2} - a_{k-1/2}$. Since the top and bottom model boundaries are material as well as coordinate surfaces, the boundary conditions are

$$\dot{\eta}_{1/2} = \dot{\eta}_{K+1/2} = 0. \tag{3.2}$$

Note that the model conserves mass due to the flux form of the continuity Eq. (3.1).

c. Pressure-gradient forces

From (2.10b), the discrete VPGF is given by

$$(\text{VPGF})_{k+1/2} = -g\theta_{k+1/2}\frac{\Pi_{k+1} - \Pi_k}{\tilde{\phi}_{k+1} - \tilde{\phi}_k} \quad \text{for } k = 1, 2, \cdots, K-1, \tag{3.3}$$

and

$$(\text{VPGF})_{1/2} = -g\theta_{1/2}\frac{\Pi_1 - \hat{\Pi}_{1/2}}{\tilde{\phi}_1 - \phi_{1/2}}, \tag{3.4}$$

where the layer-center geopotential is interpolated as

$$\tilde{\phi}_k \equiv \frac{1}{2}(\phi_{k+1/2} + \phi_{k-1/2}) \quad \text{for } k = 1, 2, \cdots, K. \tag{3.5}$$

From (2.6b), the discrete horizontal pressure-gradient force (HPGF) is given by

$$(\mathbf{HPGF})_k = -\tilde{\theta}_k\nabla\Pi_k + \frac{1}{g}\widetilde{\left(g\theta\frac{\partial\Pi}{\partial\phi}\nabla\phi\right)}_k \quad \text{for } k = 1, 2, \cdots, K, \tag{3.6}$$

where

$$\widetilde{\left(g\theta\frac{\partial\Pi}{\partial\phi}\nabla\phi\right)}_k = -\frac{1}{2}[(\text{VPGF})_{k+1/2}\nabla\phi_{k+1/2} + (\text{VPGF})_{k-1/2}\nabla\phi_{k-1/2}] \quad \text{for } k = 1, 2, \cdots, K-1, \tag{3.7}$$

$$\widetilde{\left(g\theta\frac{\partial\Pi}{\partial\phi}\nabla\phi\right)}_K = -\frac{1}{2}[(\text{VPGF})_{K-1/2}\nabla\phi_{K-1/2}], \tag{3.8}$$

and

$$\tilde{\theta}_k = \frac{1}{2}(\theta_{k+1/2} + \theta_{k-1/2}) \quad \text{for } k = 1, 2, \cdots, K. \tag{3.9}$$

In the appendix, we show that the averaging used in (3.5) and (3.9) is necessary to satisfy an integral constraint on the total energy conservation.

The upper boundary is assumed to be a constant-height surface; therefore, $w_{K+1/2} = 0$. The vertical velocity at the lower boundary is diagnosed from

$$w_{1/2} = \frac{1}{g}(\mathbf{v}_1 \cdot \nabla\phi_{1/2}), \tag{3.10}$$

which comes from the boundary condition (2.11). Using (3.10), the horizontal and vertical tendencies are related by

$$\frac{\partial w_{1/2}}{\partial t} = \frac{1}{g}\left(\frac{\partial\mathbf{v}_1}{\partial t}\cdot\nabla\phi_{1/2}\right). \tag{3.11}$$

From (2.9), we express the tendency of $w_{1/2}$ as

$$\frac{\partial w_{1/2}}{\partial t} = (\text{VPGF})_{1/2} - g + (F_z)_{1/2} - \left(\mathbf{v}\cdot\nabla w + \dot{\eta}\frac{\partial w}{\partial\eta}\right)_{1/2}. \tag{3.12}$$

As mentioned above, $w_{1/2}$ is a diagnosed quantity; therefore, (3.12) is not used as a prognostic equation in the model. Instead, it is used to diagnose the surface pressure. Equations (3.4), (3.7), (3.11), and (3.12) can be solved for the unknown $(\text{VPGF})_{1/2}$ (see Toy 2008). The surface pressure is then diagnosed from (3.4) by way of the surface Exner function.

d. Thermodynamic energy equation

The vertically discrete prognostic equation for θ is based on (2.12), except with the vertical advection term expressed as $(m\Pi)^{-1}[\partial(m\dot{\eta}\Pi\theta)/\partial\eta - \theta\ \partial(m\dot{\eta}\Pi)/\partial\eta]$. This term is written in centered form in the discrete equation, which is given by

$$\frac{\partial\theta_{k+1/2}}{\partial t} + \frac{(m\Pi\mathbf{v}\delta\eta)_{k+1/2}}{(m\Pi\delta\eta)_{k+1/2}}\cdot\nabla\theta_{k+1/2} + \frac{(m\dot{\eta})_{k+1}(\Pi\tilde{\theta})_{k+1} - (m\dot{\eta})_k(\Pi\tilde{\theta})_k}{(m\Pi\delta\eta)_{k+1/2}} - \theta_{k+1/2}\frac{\Pi_{k+1}(m\dot{\eta})_{k+1} - \Pi_k(m\dot{\eta})_k}{(m\Pi\delta\eta)_{k+1/2}} = \frac{(mQ\delta\eta)_{k+1/2}}{(m\Pi\delta\eta)_{k+1/2}} \quad \text{for } k = 1, 2, \cdots, K-1, \tag{3.13}$$

$$\frac{\partial\theta_{1/2}}{\partial t}+\frac{(m\mathbf{v})_1}{m_1}\cdot\nabla\theta_{1/2}+\frac{(\tilde{\theta}_1-\theta_{1/2})(m\dot{\eta})_1}{m_{1/2}(\delta\eta)_{1/2}}=\frac{Q_{1/2}}{\Pi_1}, \tag{3.14}$$

and

$$\frac{\partial\theta_{K+1/2}}{\partial t}+\frac{(m\mathbf{v})_K}{m_K}\cdot\nabla\theta_{K+1/2}+\frac{(\theta_{K+1/2}-\tilde{\theta}_K)(m\dot{\eta})_K}{m_{K+1/2}(\delta\eta)_{K+1/2}}=\frac{Q_{K+1/2}}{\Pi_K}, \tag{3.15}$$

where

$$(m\Pi\delta\eta)_{k+1/2}\equiv\frac{1}{2}[(m\Pi)_k(\delta\eta)_k+(m\Pi)_{k+1}(\delta\eta)_{k+1}] \quad \text{for } k=1,\,2,\cdots,\,K-1, \tag{3.16}$$

and

$$(m\Pi\mathbf{v}\delta\eta)_{k+1/2}\equiv\frac{1}{2}[\Pi_k(m\mathbf{v})_k(\delta\eta)_k+\Pi_{k+1}(m\mathbf{v})_{k+1}(\delta\eta)_{k+1}] \quad \text{for } k=1,\,2,\cdots,\,K-1. \tag{3.17}$$

Note that this form of the thermodynamic equation is similar to that of KA97. It is dictated by the CP-grid staggering and total energy conservation considerations discussed in the appendix.

e. Geopotential tendency equation

The tendency equation for the geopotential is written as

$$\frac{\partial\phi_{k+1/2}}{\partial t}+\frac{(m\mathbf{v})_{k+1/2}}{m_{k+1/2}}\cdot\nabla\phi_{k+1/2}+\dot{\eta}_{k+1/2}\frac{\tilde{\phi}_{k+1}-\tilde{\phi}_k}{(\delta\eta)_{k+1/2}}=gw_{k+1/2} \quad \text{for } k=1,\,2,\cdots,\,K-1, \tag{3.18}$$

where the layer-edge horizontal mass fluxes are given by (A.12) in the appendix.

f. Diagnostic relations

The density at layer centers is diagnosed from the pseudodensity and geopotential using the discrete form of (2.3) given by

$$\rho_k=\frac{m_k g(\delta\eta)_k}{\phi_{k+1/2}-\phi_{k-1/2}} \quad \text{for } k=1,\,2,\cdots,\,K. \tag{3.19}$$

The diagnostic equation for temperature at layer centers is obtained from (2.8) and is based on the potential temperature interpolated to layer centers. It is written as

$$T_k=\frac{\tilde{\theta}_k\Pi_k}{c_p} \quad \text{for } k=1,\,2,\cdots,\,K. \tag{3.20}$$

The ideal gas law, which relates layer-center state variables, is written as

$$p_k=\rho_k RT_k \quad \text{for } k=1,\,2,\cdots,\,K, \tag{3.21}$$

and the Exner function is given by

$$\Pi_k=c_p\left(\frac{p_k}{p_0}\right)^{\kappa} \quad \text{for } k=1,\,2,\cdots,\,K. \tag{3.22}$$

Given the density from (3.19), the temperature, the pressure, and the Exner function are solved simultaneously from (3.20)–(3.22).

g. Diagnosis of the generalized vertical velocity

The generalized vertical velocity is diagnosed through a multistep process. The first step is to calculate the target-seeking contribution $\dot{\eta}_T$ from the discrete forms of (2.28), (2.31), and (2.33), given by

$$(\dot{\eta}_T)_{k+1/2}=\begin{cases}\dfrac{(\delta\eta)_{k+1/2}}{(\delta F)_{k+1/2}}\left\{\left[\left(\dfrac{\partial F}{\partial\theta}\right)_\sigma\left(\dfrac{Q}{\Pi}-\mathbf{v}\cdot\nabla\theta\right)+\left(\dfrac{\partial F}{\partial\sigma}\right)_\theta\dfrac{1}{H}(w-\mathbf{v}\cdot\nabla z)\right]_{k+1/2}\right. & \\ \qquad\left.+\dfrac{F(\theta_{k+1/2},\sigma_{k+1/2})-\eta_{k+1/2}}{\tau_{\rm rel}}\right\}, & \text{for } \dfrac{(\delta F)_{k+1/2}}{(\delta\eta)_{k+1/2}}\ge\beta; \\ \left[1-\dfrac{1}{\beta}\dfrac{(\delta F)_{k+1/2}}{(\delta\eta)_{k+1/2}}\right]\dfrac{(\delta\eta)_{k+1/2}}{(\delta z)_{k+1/2}}(w-\mathbf{v}\cdot\nabla z)_{k+1/2}+\dfrac{1}{\beta^2}\dfrac{(\delta F)_{k+1/2}}{(\delta\eta)_{k+1/2}}\left\{\left[\left(\dfrac{\partial F}{\partial\theta}\right)_\sigma\left(\dfrac{Q}{\Pi}-\mathbf{v}\cdot\nabla\theta\right)\right.\right. & \\ \qquad\left.\left.+\left(\dfrac{\partial F}{\partial\sigma}\right)_\theta\dfrac{1}{H}(w-\mathbf{v}\cdot\nabla z)\right]_{k+1/2}+\dfrac{F(\theta_{k+1/2},\sigma_{k+1/2})-\eta_{k+1/2}}{\tau_{\rm rel}}\right\}, & \text{for } 0<\dfrac{(\delta F)_{k+1/2}}{(\delta\eta)_{k+1/2}}<\beta; \\ \dfrac{(\delta\eta)_{k+1/2}}{(\delta z)_{k+1/2}}(w-\mathbf{v}\cdot\nabla z)_{k+1/2}, & \text{for } \dfrac{(\delta F)_{k+1/2}}{(\delta\eta)_{k+1/2}}<0.\end{cases} \tag{3.23}$$

The next step is to calculate the smoothing contribution $\dot{\eta}_S$ which is based on the parameters $(\nabla^4 z)_{k+1/2}$ and $(\delta^2 z/\delta z)_{k+1/2}$, given by (2.23). The discrete form of (2.34) is used, which is

$$(\dot{\eta}_S)_{k+1/2} = -\left[\left(\frac{\partial z}{\partial t}\right)_{\substack{\text{smoothing,}\\ \text{horiz}}} + \left(\frac{\partial z}{\partial t}\right)_{\substack{\text{smoothing,}\\ \text{vert}}}\right]_{k+1/2} \frac{(\delta\eta)_{k+1/2}}{(\delta z)_{k+1/2}}, \tag{3.24}$$

where, from (2.35) and (2.36), we use

$$\left[\left(\frac{\partial z}{\partial t}\right)_{\substack{\text{smoothing,}\\ \text{horiz}}}\right]_{k+1/2} = -\max\{0, \kappa_{\text{horiz}}[|\nabla^4 z|_{k+1/2} - (\nabla^4 z)_{\max}]\}\text{sgn}(\nabla^4 z)_{k+1/2} \tag{3.25}$$

and

$$\left[\left(\frac{\partial z}{\partial t}\right)_{\substack{\text{smoothing,}\\ \text{vert}}}\right]_{k+1/2} = \max\left\{0, \kappa_{\text{vert}}\left[\left|\frac{\delta^2 z}{\delta z}\right|_{k+1/2} - \left(\frac{\delta^2 z}{\delta z}\right)_{\max}\right]\right\}\text{sgn}\left(\frac{\delta^2 z}{\delta z}\right)_{k+1/2}. \tag{3.26}$$

Note that the smoothing contribution is generally zero except where it is necessary to advectively adjust the position of coordinate surfaces to maintain the smoothness criteria.

The final steps are to predict provisional values of the potential temperature and geopotential height based on the sum of the vertical velocity contributions given by (3.23) and (3.24). Following this, the function $F(\theta, \sigma)$ is calculated using these provisional values, and it is compared to the target F field for the current time step. A final vertical advective adjustment is then calculated to bring F to its target through an iterative procedure similar to that used by KA97. We refer to the generalized vertical velocity contribution from this adjustment procedure as $\dot{\eta}_{\text{ADJ}}$. It is generally a small, residual contribution that results from the vertical discretization and reduces to zero for infinite resolution.

The provisional values for θ and z are calculated from

$$\theta^*_{k+1/2} = \theta^n_{k+1/2} + \Delta t\left[\frac{Q}{\Pi} - \mathbf{v}\cdot\nabla\theta - (\dot{\eta}_T + \dot{\eta}_S)\frac{\partial\theta}{\partial\eta}\right]_{k+1/2} \tag{3.27}$$

and

$$z^*_{k+1/2} = z^n_{k+1/2} + \Delta t\left[w - \mathbf{v}\cdot\nabla z - (\dot{\eta}_T + \dot{\eta}_S)\frac{\partial z}{\partial\eta}\right]_{k+1/2}, \tag{3.28}$$

where the superscript asterisks (*) refer to the provisional values, n refers to the current time step, and Δt is the time-step length. Euler forward time stepping is shown for simplicity. From these values, we calculate

$$F^*_{k+1/2} \equiv F(\theta^*_{k+1/2}, \sigma^*_{k+1/2}), \tag{3.29}$$

where

$$\sigma^*_{k+1/2} = \frac{z^*_{k+1/2} - z_S}{z_T - z_S}. \tag{3.30}$$

The target value for F at time step $n + 1$ is calculated from the prognostic equation

$$F^{n+1,\text{TARGET}}_{k+1/2} = F^n_{k+1/2} + (\Delta t)\frac{\eta_{k+1/2} - F^{n-1}_{k+1/2}}{\tau_{\text{rel}}}, \tag{3.31}$$

which is based on (2.20) with $\dot{\eta}_S$ set to zero. Equation (3.31) is designed to relax $F^{n+1,\text{TARGET}}_{k+1/2}$ toward the vertical coordinate value $\eta_{k+1/2}$. The difference between the provisional and target values of F is then defined as

$$(\Delta\eta)_{k+1/2} \equiv F^*_{k+1/2} - F^{n+1,\text{TARGET}}_{k+1/2}. \tag{3.32}$$

The purpose of $(\dot{\eta}_{\text{ADJ}})_{k+1/2}$ is to bring $(\Delta\eta)_{k+1/2}$ to zero, which, at each iteration, is solved from

$$(\Delta\eta)_{k+1/2} = \Delta t\left\{\left[\left(\frac{\partial F^*}{\partial\theta^*}\right)_\sigma\right]_{k+1/2}(\dot{\eta}_{\text{ADJ}})_{k+1/2}\frac{(\delta\theta)_{k+1/2}}{(\delta\eta)_{k+1/2}} + \left[\left(\frac{\partial F^*}{\partial\sigma^*}\right)_\theta\right]_{fk+1/2}(\dot{\eta}_{\text{ADJ}})_{k+1/2}\frac{(\delta\sigma)_{k+1/2}}{(\delta\eta)_{k+1/2}}\right\}. \tag{3.33}$$

The result is used to update θ^* and σ^* from

$$\theta^*_{k+1/2} = \theta^*_{k+1/2} - \Delta t(\dot{\eta}_{\rm ADJ})_{k+1/2}\frac{(\delta\theta)_{k+1/2}}{(\delta\eta)_{k+1/2}} \qquad (3.34)$$

and

$$\sigma^*_{k+1/2} = \sigma^*_{k+1/2} - \Delta t(\dot{\eta}_{\rm ADJ})_{k+1/2}\frac{(\delta\sigma)_{k+1/2}}{(\delta\eta)_{k+1/2}}. \qquad (3.35)$$

Equations (3.29) and (3.32)–(3.35) are iterated until $\Delta\eta$ becomes sufficiently small. The final value of $(\dot{\eta}_{\rm ADJ})_{k+1/2}$ is the cumulative value calculated in each iteration. The resulting values of θ^* and σ^* are the final $n + 1$ values.

Finally, the generalized vertical velocity is given by

$$\dot{\eta}_{k+1/2} = (\dot{\eta}_T)_{k+1/2} + (\dot{\eta}_S)_{k+1/2} + (\dot{\eta}_{\rm ADJ})_{k+1/2}. \qquad (3.36)$$

Note that in the continuous limit, $\dot{\eta}_{\rm ADJ}$becomes zero, and (3.36) reduces to (2.26).

4. Results

In this section, we compare the results of the model run with the Eulerian σ coordinate versus the hybrid vertical coordinate for two-dimensional mountain-wave simulations. These tests include an idealized isothermal case, and a simulation of the 11 January 1972 Boulder, Colorado, windstorm. The two coordinate systems are compared with regard to processes such as vertical momentum and passive tracer transport, as well as wave breaking. In terms of computational overhead, we found that the hybrid-coordinate model takes approximately 15% longer to run than with the σ coordinate for a given number of time steps. This is due to the additional expense associated with coordinate smoothing and diagnosis of the vertical velocity within the hybrid-coordinate framework.

a. Small-amplitude mountain waves in an isothermal atmosphere

A simple test case is presented to demonstrate the ability of the model to represent small-amplitude gravity waves. Smith (1979) provides a review of mountain-wave theory that includes linear analytical solutions with which the model results can be compared. In the experiment, the flow is initially isothermal with a temperature of $\overline{T} = 287$K and is purely horizontal with zonal wind speed $\overline{u} = 20$ m s^{-1}. (Overbars represent the basic state.) The buoyancy frequency, given by $\overline{N} = \sqrt{(g/\overline{\theta})\partial\overline{\theta}/\partial z}$, a constant for isothermal atmospheres, is 0.0183 s^{-1}. Following Queney (1948), the mountain is an isolated barrier whose profile is prescribed as a witch of Agnesi curve given by

$$z_S(x) = \frac{h}{1 + (x/a)^2}, \qquad (4.1)$$

where $z_S(x)$ is the surface height, h is the mountain height, and a is the half-width. In this experiment, $h = 10$ m and $a = 2$ km. A measure of the linearity of the wave solution is the inverse Froude number based on the mountain height, which is Nh/u. Linear wave theory applies when the mountain is small, that is, when $Nh/\overline{u} \ll 1$. In this experiment, $Nh/\overline{u} = 0.00915 \ll 1$, so we can compare the model results to the analytic linear solution. The inverse Froude number based on the mountain half-width is given by Na/u. For broad mountains, in which $Na/\overline{u} \gg 1$, the flow is approximately hydrostatic. With narrow mountains, the hydrostatic approximation breaks down. In our case, $Na/\overline{u} = 1.83 \sim 1$, so the flow is nonhydrostatic. Figures 3a and 4a show the steady-state analytic linear solutions to the perturbation zonal and vertical velocity fields (u' and w'), respectively. Note that phase lines tilt upwind, while wave packets have a downwind tilt characteristic of nonhydrostatic flow. The solution is based on the first 90 Fourier modes of the surface topography. The lateral boundaries are periodic with a domain length of $L = 120$ km, and radiative upper boundary conditions are applied.

In the model simulations, the horizontal boundary conditions are periodic and the domain length is $L = 120$ km. The upper boundary is a rigid lid at 30 km. A Rayleigh damping layer based on Klemp and Lilly (1978) is used in the upper portion of the domain. The model is run with 120 levels and 600 horizontal grid points. For the hybrid-coordinate run, we use $\theta_{\rm min} = 270$ K, $(\partial\theta/\partial\sigma)_{\rm min} = 0$ K, and $r = 64$. As shown in Fig. 5, this provides a rapid transition with height from the terrain-following coordinate to the θ coordinate. At $z \approx 3$ km and above, the coordinate is nearly isentropic. Figures 3b and 4b show numerical model results with the σ coordinate, and Figs. 3c and 4c show results with the hybrid coordinate. Both simulations agree well with the analytical solution. For both simulations, the perturbation velocity fields are shown at time $t = 40a/\overline{u}$ (1.11 h), at which time the models reached an approximate steady state.

Linear theory provides an analytical solution to the vertical flux of horizontal momentum. Following Eliassen and Palm (1961), the momentum flux is written as

$$M(z) = \int_{-L/2}^{L/2} \overline{\rho}\, u'w'\, dx = L\,\overline{\rho}\,\overline{u'w'}, \qquad (4.2)$$

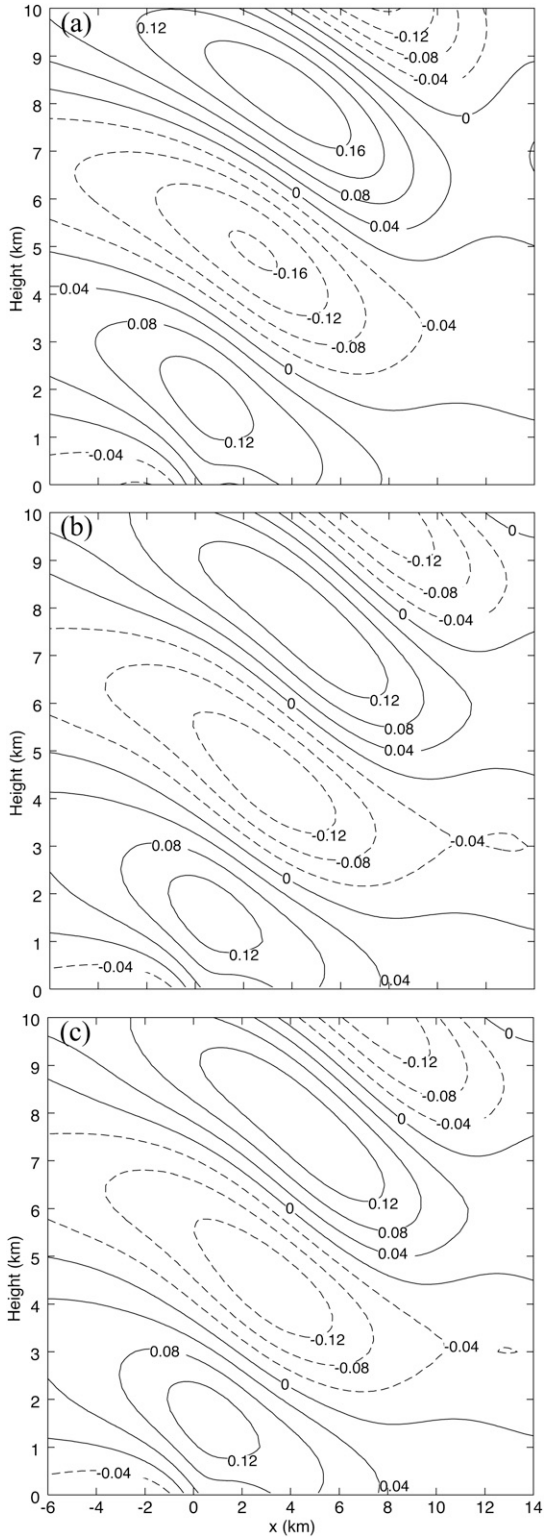

FIG. 3. Perturbation zonal wind u' (m s^{-1}) in the vicinity of the 10-m-high, 2-km half-wide mountain from (a) the steady-state analytical solution, and from simulations at $t = 40a/\overline{u}$ (1.11 h) with (b) the σ vertical coordinate and (c) the hybrid vertical coordinate. The horizontal axis represents the distance relative to the mountain center.

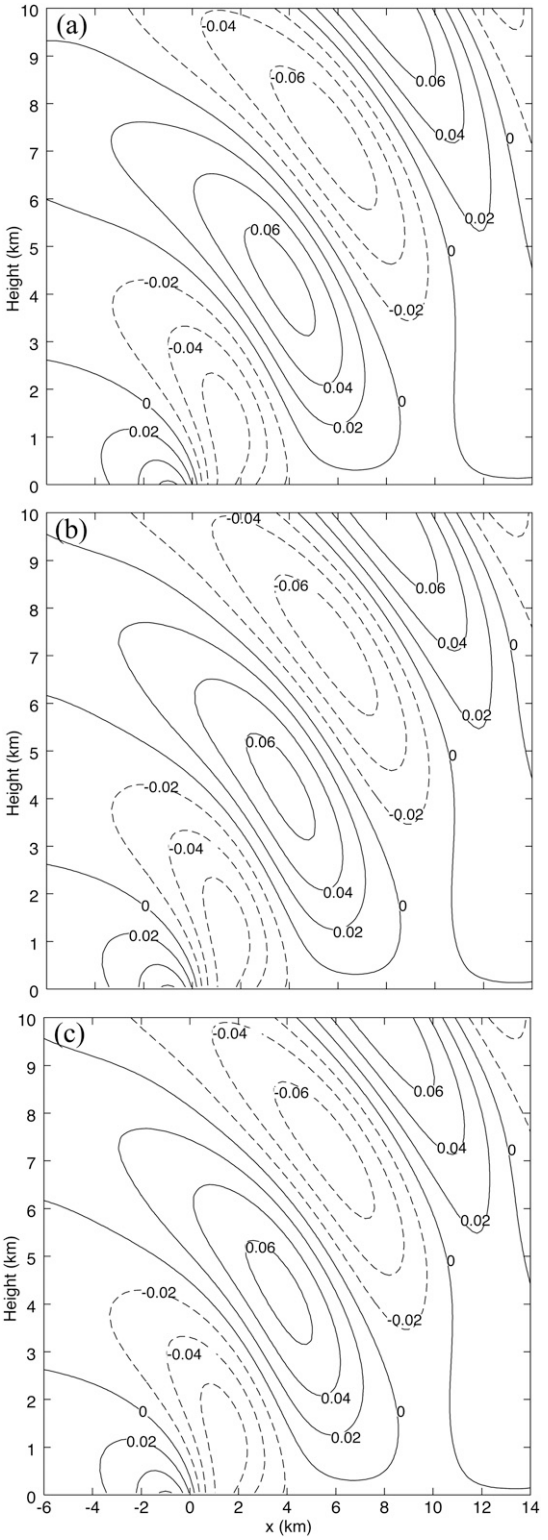

FIG. 4. As in Fig. 3 except plotted fields are the perturbation vertical velocity w' (m s^{-1}).

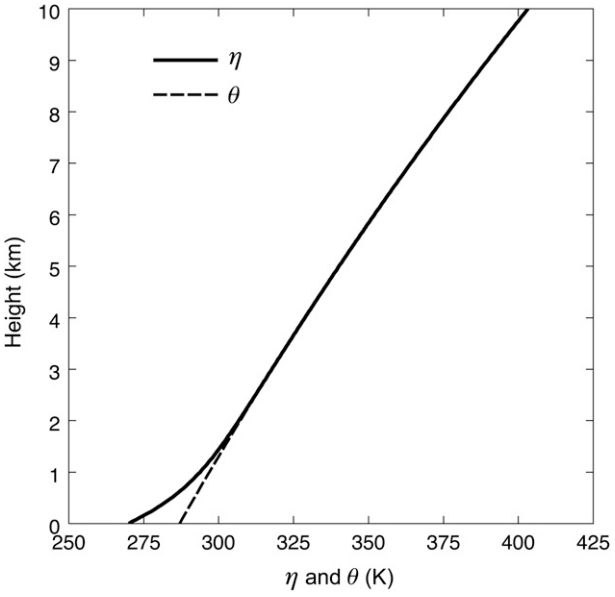

FIG. 5. Vertical profiles of the hybrid vertical coordinate (solid curve) and potential temperature (dashed curve) for the small-amplitude, isothermal mountain-wave experiment. The coordinate is isentropic above ~3 km.

which, for steady-state conditions, is constant in height. From the model runs, we diagnose the nonlinear momentum flux given by (2.51). We define two components of the momentum flux: the "eddy flux" component given by

$$M_{\mathrm{EF}}(z) \equiv \int_{-L/2}^{L/2} (m\dot{\eta})' u' \, dx = L\,\overline{(m\dot{\eta})' u'}, \tag{4.3}$$

and the "form drag" component given by

$$M_{\mathrm{FD}}(z) \equiv -\int_{-L/2}^{L/2} p' \frac{\partial z'}{\partial x} \, dx = -L\,\overline{p' \frac{\partial z'}{\partial x}}. \tag{4.4}$$

The surface pressure drag M_{SD} is equal to the form drag component evaluated along the surface; that is,

$$M_{\mathrm{SD}} \equiv M_{\mathrm{FD}}(\eta = \eta_S). \tag{4.5}$$

For steady-state flow, the following relation theoretically applies at all levels:

$$M_{\mathrm{EF}}(z) + M_{\mathrm{FD}}(z) = M_{\mathrm{SD}} = \text{constant}. \tag{4.6}$$

Figure 6 shows the vertical profiles of the eddy and form-drag contributions to the momentum flux at time $t = 40a/\overline{u}$. The sum of these, shown by the black curve, theoretically equals the surface drag. The theoretical result is plotted as the vertical red line for reference. In each coordinate system, the total momentum flux is nearly constant with height and is close to the theoretical surface-drag value, as well as the linear momentum flux given by (4.2). The sign of the total momentum flux

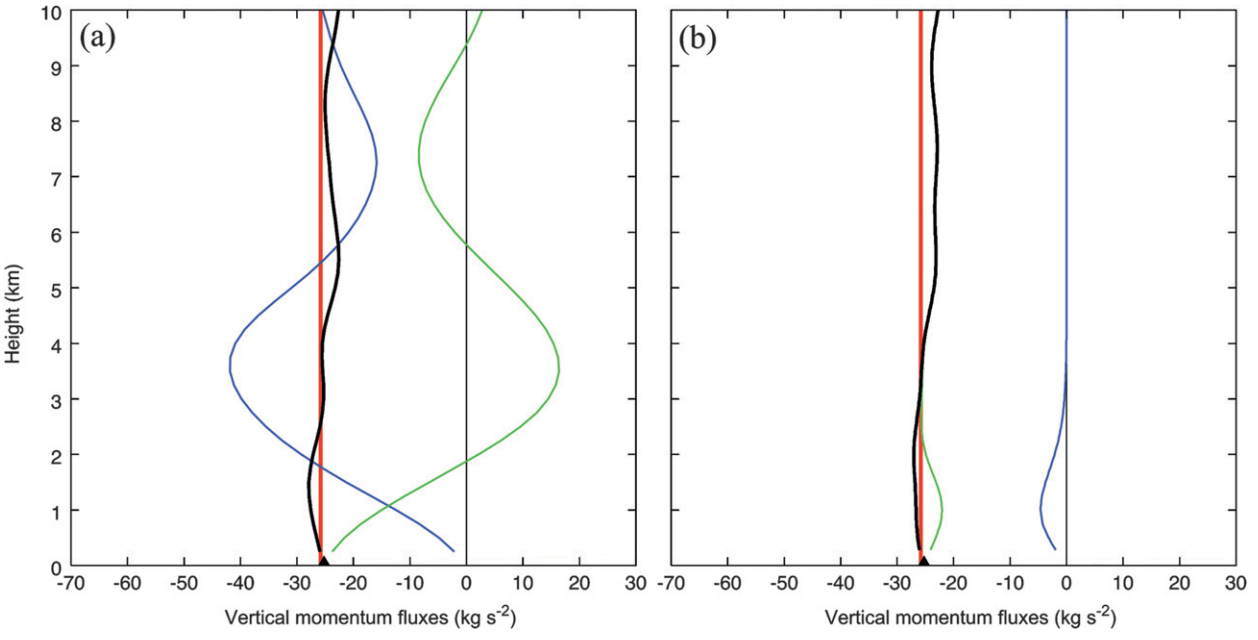

FIG. 6. Vertical flux of the horizontal momentum diagnosed from the (a) σ vertical coordinate and (b) hybrid vertical coordinate runs at $t = 40a/\overline{u}$ (1.11 h) for the small-amplitude mountain-wave experiment. The blue curves are eddy momentum fluxes M_{EF}, the green curves are the form drag M_{FD}, the black curves are the sums of these, and the red curves are the analytical, steady-state momentum fluxes from linear theory given by (4.2). The black triangles are the diagnosed surface drag M_{SD}.

is negative, which means that the surface exerts a drag on the atmosphere, as expected. Note the nonzero contribution of the form drag in σ coordinates (Fig. 6a), which is due to the sloping of the coordinate surfaces with respect to z. In the Eulerian system, the vertical variations of the eddy-flux and form-drag contributions cancel in such a way as to keep their sum approximately constant in height. With the hybrid coordinate, a simpler view of momentum transport is afforded, as the flux is due entirely to the form drag component above ~3 km. This is because the coordinate is almost purely isentropic, so the vertical velocity is zero and, therefore, the eddy flux is zero as well.

b. *The 11 January 1972 Boulder, Colorado, downslope windstorm*

The downslope windstorm that occurred in Boulder, Colorado, on 11 January 1972 was an extensively observed meteorological event (Lilly and Zipser 1972). It provides an ideal test case for model simulations of mountain-wave amplification and breaking. In this experiment, we follow Doyle et al. (2000), which presents various two-dimensional (x–z) simulations of the windstorm. The topography is idealized by a witch of Agnesi curve with the height and half-width set at $h = 2$ km and $a = 10$ km, respectively. The free-slip condition is applied at the lower boundary. The horizontal domain is 220 km in extent, and we use periodic lateral boundary conditions. The horizontal grid spacing is $\Delta x = 1$ km. The model top is a rigid lid at $z = 48$ km. In the lower 35 km, we use even vertical grid spacing in z. Above this level, the grid is stretched by gradually increasing the layer thickness up to the model top.

The baseline vertical resolution is 125 levels in the lowest 25 km, giving an average vertical grid spacing of 200 m. A high-resolution σ-coordinate run was also performed using 500 levels in the lowest 25 km. Three simulations are presented: 1) the "Sigma125" run using σ coordinates and the baseline vertical resolution, 2) the "Sigma500" run using σ coordinates and the high vertical resolution, and 3) the "Hybrid125" run using hybrid coordinates at the baseline vertical resolution. The hybrid vertical coordinate parameters introduced in (2.16), (2.18), and (2.19) were specified as $\theta_{\min} = 270$ K, $(\partial\theta/\partial\sigma)_{\min} = 0$ K, and $r = 16$. As shown in Fig. 7, the hybrid coordinate is primarily isentropic above $z = 10$ km.

In this experiment, coordinate surface smoothing is applied in the hybrid vertical coordinate runs to allow for isentropic overturning. Referring to (3.25) and (3.26), the maximum smoothness thresholds, above which smoothing occurs, are specified as $(\nabla^4 z)_{\max} = 3.4 \times 10^{-11}$ m^{-3} and $(\delta^2 z/\delta z)_{\max} = 0.4$. The diffusion

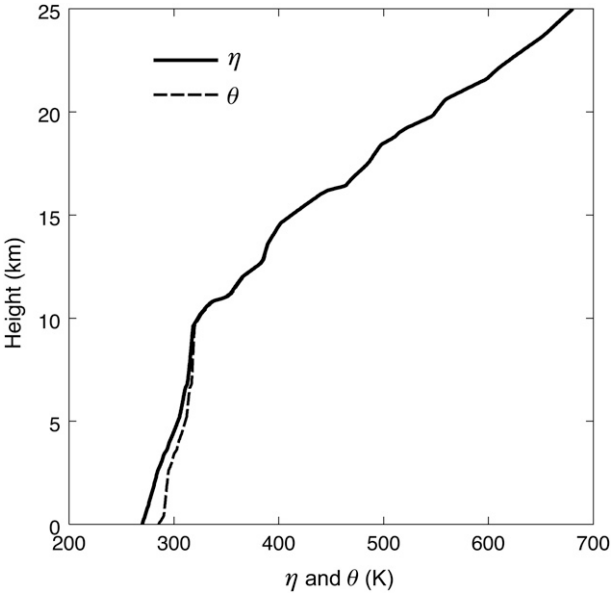

FIG. 7. Vertical profiles of the hybrid vertical coordinate (solid curve) and potential temperature (dashed curve) at the initial time for the Hybrid125 simulation of the 11 Jan 1972 Boulder downslope windstorm.

coefficients used for horizontal and vertical smoothing are $\kappa_{\text{horiz}} = 3.125 \times 10^{12}$ m^4 s^{-1} and $\kappa_{\text{vert}} = 1000$ m s^{-1}, respectively. On two-gridpoint length scales, these coefficients correspond to e-folding times of $O(10^{-2}$ s); that is, the smoothing acts on a short time scale. (This is on the order of the model time steps, which, for now, is limited by vertically propagating acoustic waves and the use of an explicit time-differencing scheme: third-order Adams–Bashforth.) The relaxation time constant introduced in (2.20) is specified as $\tau_{\text{rel}} = 0.5$ h, which is on the order of the time scale on which the wave breaking occurs. Finally, the parameter β used in (3.23) is set to 0.7.

We apply a subgrid-scale mixing parameterization to the three components of velocity as well as the potential temperature, following the scheme used in the University of Oklahoma's Advanced Research Prediction System (ARPS; documentation available online at http://www.caps.ou.edu/ARPS/download/code/pub/ARPS.docs/ARPS4DOC.PDF/arpsch6.pdf). We use the modified Smagorinsky first-order closure scheme (Smagorinsky 1963), which includes Richardson number dependency.

The initial conditions, shown in Fig. 8, are uniform in the horizontal following Doyle et al. (2000). They are based on the upstream 1200 UTC 11 January 1972 Grand Junction, Colorado, sounding up to 25 km. At higher levels, a constant zonal wind of 7.5 m s^{-1} is assumed and the temperature profile smoothly merges with that of the *U.S. Standard Atmosphere, 1976*. The reference surface pressure corresponding to $z = 0$ is 850 mb.

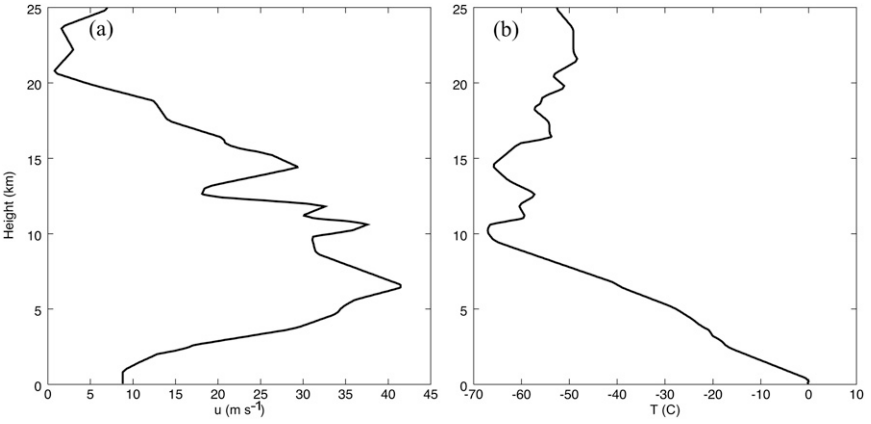

FIG. 8. Vertical profiles of the (a) zonal wind and (b) temperature used as the initial condition for the 11 Jan 1972 Boulder downslope windstorm simulation. The data are from Doyle et al. (2000) and are based on the 1200 UTC 11 Jan 1972 Grand Junction sounding.

The potential temperature field at $t = 70$ min is shown in Fig. 9. The mountain wave has substantially developed throughout the troposphere and lower stratosphere with generally an upwind tilt to the phase lines. A hydraulic jump feature has developed in the lower troposphere, approximately 20 km downstream of the mountaintop with lee waves of horizontal wavelength ~10 km appearing just downstream. There is also considerable wave development above the hydraulic jump at the base of the stratosphere, with lee waves appearing just downstream as well.

The three simulations shown in Fig. 9 agree well with each other. The most noticeable difference is that in the σ-coordinate runs, isentropes are already beginning to overturn at the 19-km level. This overturning is more pronounced in the Sigma500 run. In the Hybrid125 run, overturning has not occurred yet, which is likely due to the decreased resolution of the isentropic coordinate in the areas of low static stability. Coordinate surfaces closely follow the isentropes above ~10 km.

A particular advantage of the isentropic coordinate is the enhancement of vertical resolution in regions of high static stability. As shown in Fig. 10, which shows the static stability field at $t = 2$ h, this advantage leads to more accurately resolved layers of stable air. This was also recently noted by Zängl (2007), who found improved representation of the tropopause in nonhydrostatic simulations with the isentropic coordinate. The static stability field resulting from the Hybrid125 simulation (Fig. 10c) closely resembles that of the high vertical resolution Sigma500 run (Fig. 10a) in terms of capturing layers of high static stability. In the Sigma125 run (Fig. 10b), these layers are much less pronounced. Use of the hybrid coordinate, therefore, provides an economic advantage over the σ coordinate by capturing these features with the same number of model layers. On the other hand, Fig. 10 shows that the hybrid coordinate underestimates the degree of static instability in regions of wave breaking. As mentioned before, this is likely due to the reduced vertical resolution in these regions.

At 3 h of simulation time, the wave-breaking activity is at a maximum, as is the surface-wind intensity on the leeward mountain slope, that is, the simulated downslope windstorm. The potential temperature and zonal wind fields at this time are shown in Figs. 11 and 12, respectively. There is general agreement among the three model configurations. These results also compare well with the model results presented in Doyle et al. (2000; see Figs. 3 and 4 of their paper).

The diagnosed surface form drag, given by $D = -\oint_x p_S(\partial z_S/\partial x)dx$, is plotted as a time series in Fig. 13. The evolution of the drag force is related to the downward transfer of zonal momentum due to the amplification and breaking of the mountain wave (e.g., Peltier and Clark 1979; Durran and Klemp 1983). As shown in Fig. 13, the three simulations produced similar results during the first 1.5 simulated hours, which is the period of wave amplification that precedes wave breaking. After this time, differences develop among the runs, but they generally follow a similar evolution. For the hybrid-coordinate simulation, this indicates that the process of wave amplification and breaking is adequately represented in terms of the vertical transfer of zonal momentum. After the peak at 3 h, the drag dies out and even becomes negative for a brief period. This is due to the periodic lateral boundaries and the fact that the momentum field is not forced.

The most striking difference between the hybrid- and σ-coordinate runs is in the vertical advection of a passive tracer. Here, we see a distinct advantage with the

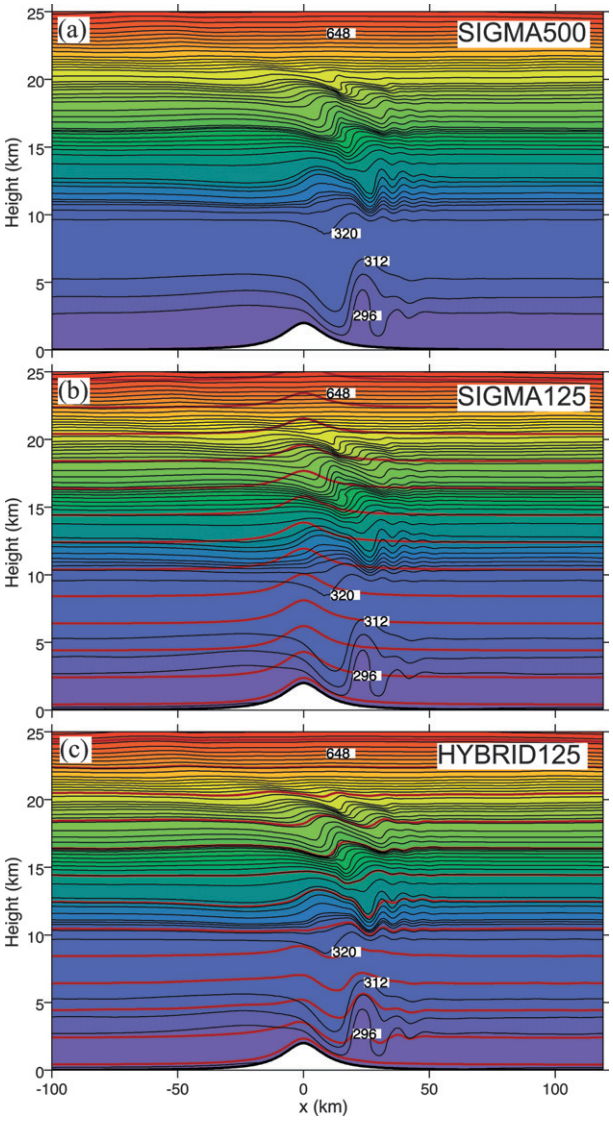

FIG. 9. Potential temperature (black contours and shading) at time $t = 1$ h 10 min for the 11 Jan 1972 Boulder downslope windstorm simulations using the σ coordinate with (a) 500 and (b) 125 levels in the lowest 25 km, and (c) the hybrid coordinate with 125 levels in the lowest 25 km. The contour interval is 8 K, and selected isentropes are labeled. The boldface red curves in (b) and (c) indicate every 10th model coordinate surface.

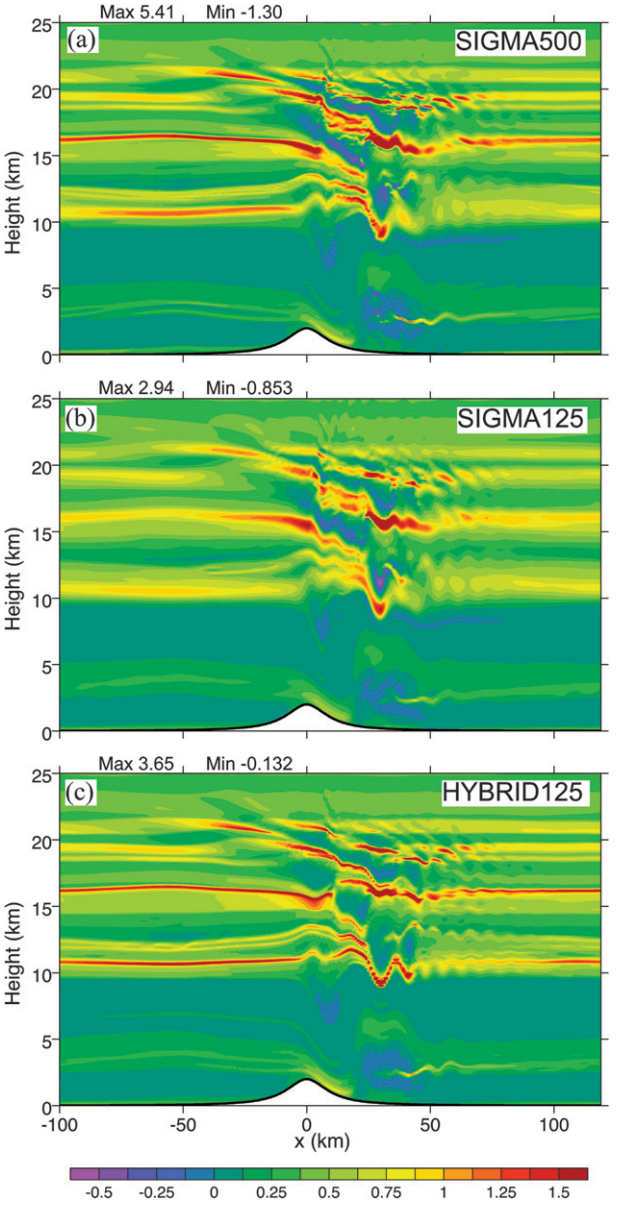

FIG. 10. Static stability $N^2 = g\theta^{-1}\partial\theta/\partial z$ (10^{-3} s^{-2}) at time $t = 2$ h for the 11 Jan 1972 Boulder downslope windstorm simulations using the σ coordinate with (a) 500 and (b) 125 levels in the lowest 25 km, and (c) the hybrid coordinate with 125 levels in the lowest 25 km.

isentropic coordinate. To isolate the effects of vertical advection as much as possible, the passive tracer is initialized along horizontal bands bounded by selected isentropes as shown in Fig. 14a. The tracer is assigned the arbitrary value of unity inside the bands and zero outside. This is also shown in a scatterplot of tracer concentration versus potential temperature for all model points, as shown in Fig. 14b. In the continuous system of equations for adiabatic processes, since θ is conserved, the correlation between θ and the passive tracer remains unchanged in time assuming no diffusion of either property. This means that the scatterplot of tracer concentration versus θ should remain unchanged in time.

Profiles of the tracer concentration after 70 min of simulation time are shown in Fig. 15. In contrast to the initial conditions shown in Fig. 14a, there are now additional values of tracer concentration besides 0 and 1, and some of the tracer has ''leaked'' outside of the original isentropic bounds indicated by the boldface black curves. This has occurred because of numerical

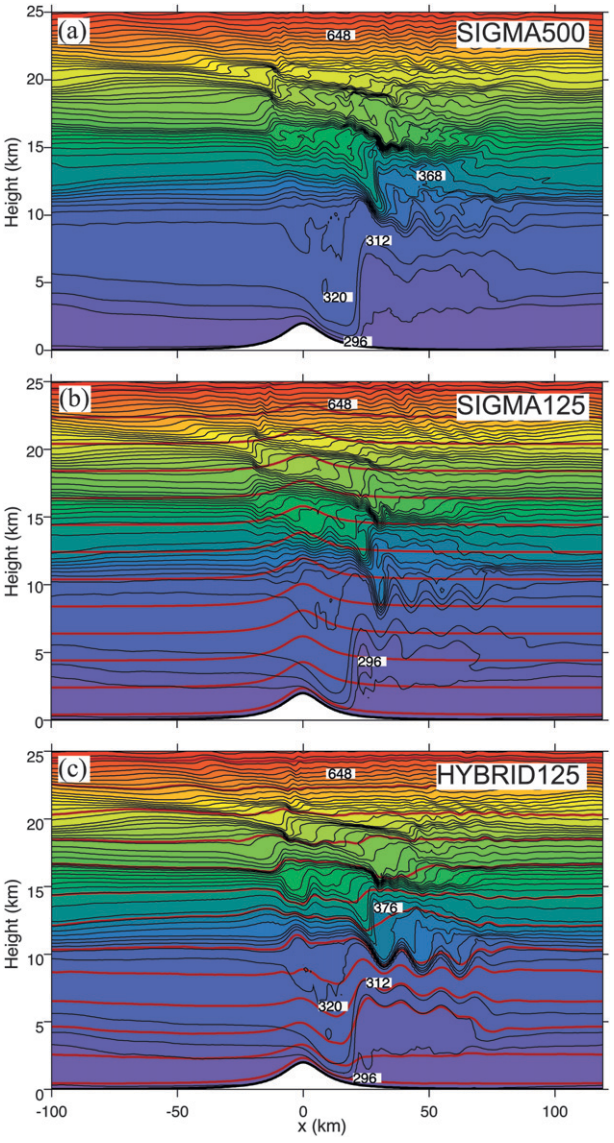

FIG. 11. As in Fig. 9 but at time $t = 3$ h.

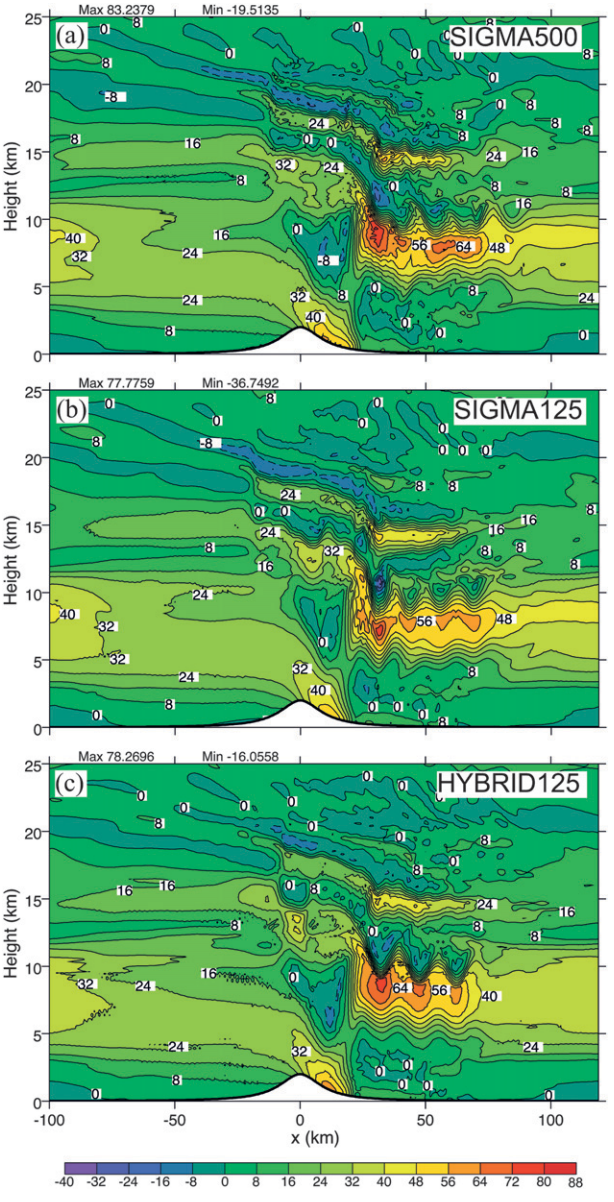

FIG. 12. Zonal wind (m s^{-1}) at time $t = 3$ h for the 11 Jan 1972 Boulder downslope windstorm simulations using the σ coordinate with (a) 500 and (b) 125 levels in the lowest 25 km, and (c) the hybrid coordinate with 125 levels in the lowest 25 km. The contour interval is 8 m s^{-1}.

dispersion associated with the vertical advection terms of the tracer tendency equation. The dispersion error is most evident where the coordinate is σ, that is, in Figs. 15a and 15b and the lowest band in the hybrid coordinate plot in Fig. 15c. At $t = 70$ min, wave overturning has not yet occurred and there has been minimal coordinate smoothing in the hybrid vertical coordinate run. Therefore, the vertical velocity in the θ-coordinate regions of the hybrid coordinate has been virtually zero up until this time. The effect of this can be seen in the upper three tracer bands in Fig. 15c as compared to those in Figs. 15a and 15b.

The characteristics mentioned above are more noticeable in Fig. 16. The difference between the top tracer band among the four simulations is the most striking. With the hybrid coordinate (Fig. 16c), the scatter points lie along the theoretical profile indicated by the dashed lines. In the 125-level σ-coordinate simulation (Fig. 16b), the profile of the upper band differs significantly from theoretical profile due to dispersion error and numerical diffusion. The 125-level hybrid-coordinate model also has an advantage over the high-resolution 500-level σ-coordinate simulation (Fig. 16a), in which some

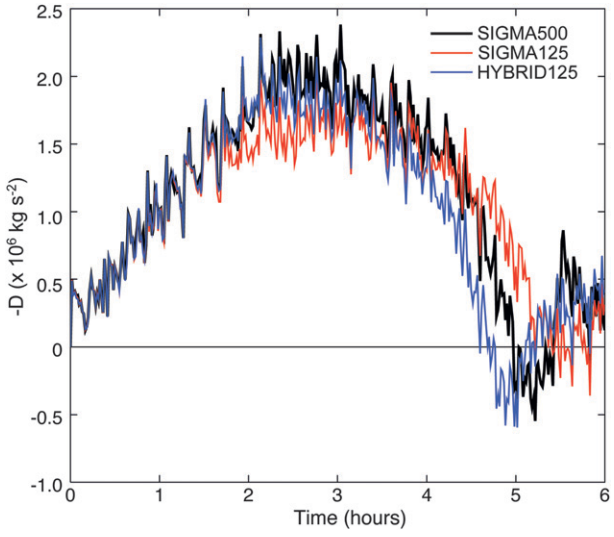

FIG. 13. Time series of the surface pressure drag for the 11 Jan 1972 Boulder downslope windstorm simulations using the σ coordinate with 500 (black curve) and 125 levels (red curve) in the lowest 25 km, and the hybrid coordinate with 125 levels in the lowest 25 km (blue curve).

dispersion is evident at the discontinuities in the original profile.

Figure 17 shows scatterplots after three simulated hours. The hybrid run displays some dispersion error due to the vertical velocity induced by coordinate smoothing. Despite this, the hybrid run exhibits less error than the Sigma125 runs. The error is comparable to, if not better than, the high-resolution Sigma500 runs, but achieves this with fewer model levels.

5. Summary and conclusions

We have developed a new nonhydrostatic, hybrid-vertical-coordinate atmosphere model that uses the quasi-Lagrangian θ coordinate throughout much of the domain. The coordinate is based on Konor and Arakawa (1997), in which the coordinate is specified as a combination of a terrain-following σ coordinate and potential temperature θ. We modified their method by incorporating adaptive grid techniques to allow the representation of negative static stability (i.e., $\partial\theta/\partial z < 0$), which develops through processes such as gravity wave breaking. In the free atmosphere, coordinate and isentropic surfaces coincide as long as specific criteria regarding the spatial arrangement of the coordinate surfaces are met. When these surfaces become irregular, mass is vertically exchanged between layers to maintain layer separation and smoothness. With the return to positive static stability, the coordinate surfaces are relaxed back to their isentropic targets.

Small-amplitude gravity wave simulations demonstrated the quasi-Lagrangian characteristics of vertical momentum transport in θ coordinates. This transport manifests itself as the balance of the pressure form drag acting on coordinate surfaces, which is a physically direct representation of the process, in contrast to the eddy flux transport within the Eulerian framework.

A simulation of the 11 January 1972 Boulder, Colorado, downslope windstorm was performed. Use of the hybrid coordinate resulted in superior performance over the σ coordinate in reducing the error associated

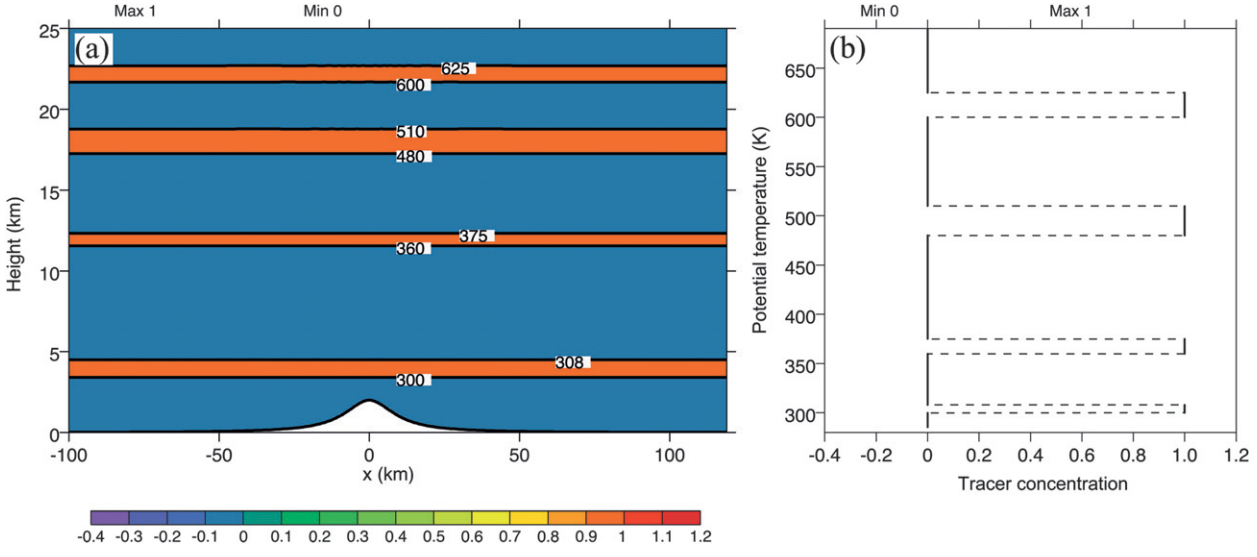

FIG. 14. (a) Contour plot of the initial passive tracer concentration (shading) and the isentropes bounding the tracer bands (black curves). (b) Scatterplot at $t = 0$ of the tracer concentration vs potential temperature. The dashed black lines indicate the theoretical scattering distribution.

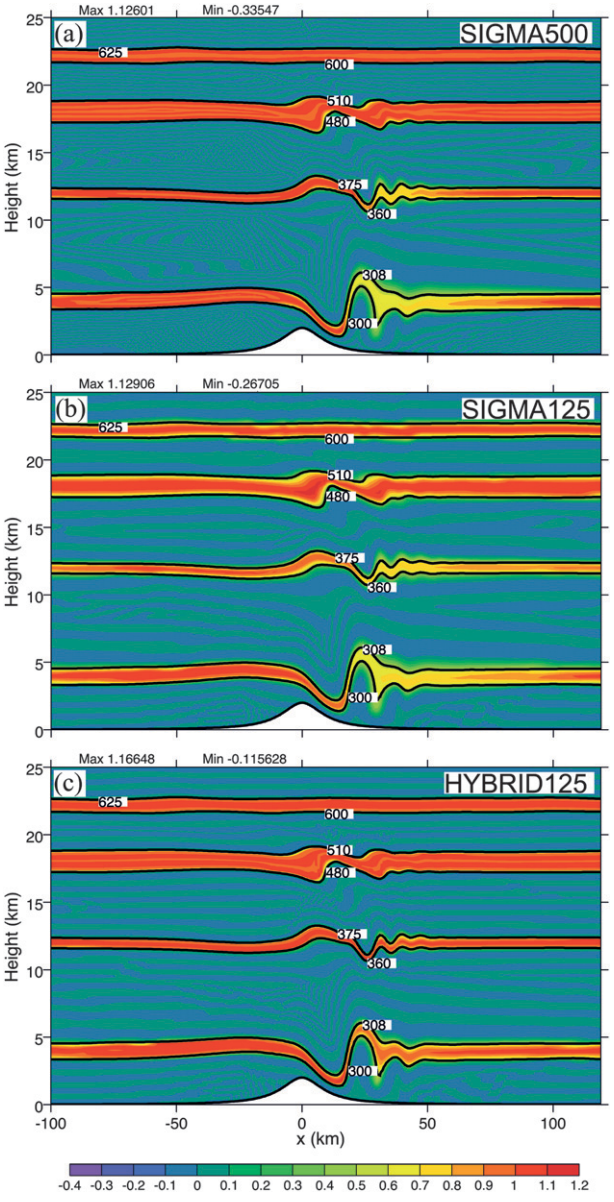

FIG. 15. Contour plots at time $t = 1$ h 10 min of the passive tracer concentration (shading) and the isentropes that originally bounded the tracer bands (black curves) using the σ coordinate with (a) 500 and (b) 125 levels in the lowest 25 km, and (c) the hybrid coordinate with 125 levels in the lowest 25 km.

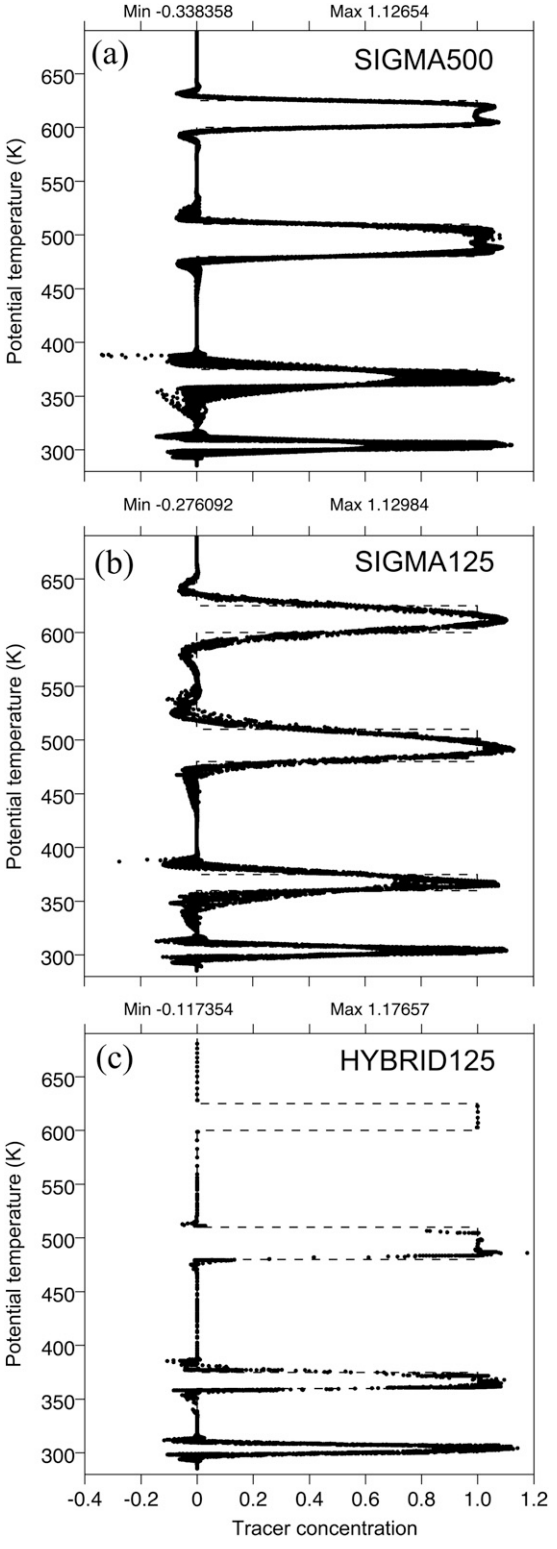

FIG. 16. Scatterplots at time $t = 1$ h 10 min of the passive tracer concentration vs potential temperature using the σ coordinate with (a) 500 and (b) 125 levels in the lowest 25 km, and (c) the hybrid coordinate with 125 levels in the lowest 25 km. The dashed black lines indicate the theoretical scattering distribution.

with the vertical transport of a passive tracer. This is due to the elimination of the vertical velocity in isentropic coordinates. Also, features of high static stability were better resolved due to the concentration of model layers that develops in regions of high static stability with the θ coordinate. On the other hand, the degree of isentropic overturning associated with wave breaking was somewhat suppressed with the hybrid coordinate. This is likely due to the decrease in vertical resolution in these

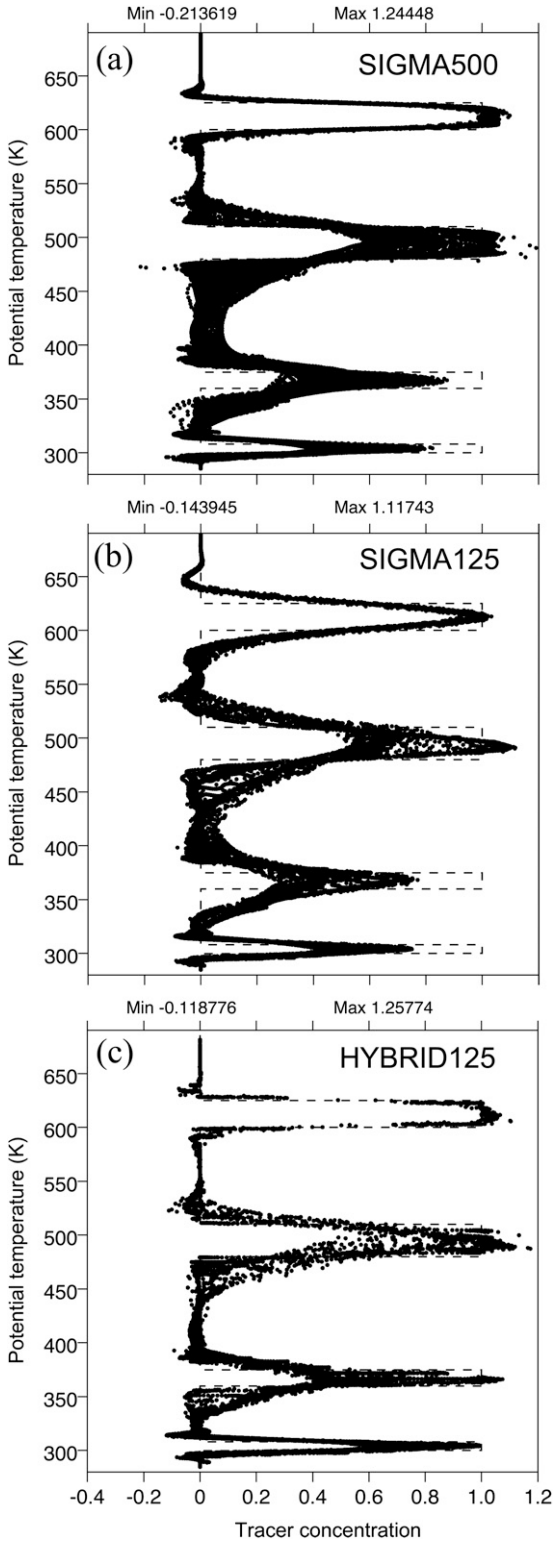

FIG. 17. As in Fig. 16 but at time $t = 3$ h.

regions resulting from the larger vertical separation of the isentropic surfaces.

Nonhydrostatic atmospheric models using potential temperature as the vertical coordinate have been successfully developed in the past decade. The model presented in this paper further demonstrates the feasibility of representing finescale motion in isentropic coordinates. This framework has distinct advantages, which are open to future development and application.

Acknowledgments. This paper is based on part of the Ph.D. dissertation by the first author at Colorado State University. The research was supported by the Office of Science (BER), U.S. Department of Energy, Grant DE-FC02-06ER64302. The first author would like to thank Dr. Celal Konor for his help and encouragement during the development of the model. We wish to thank the reviewers for their valuable comments, which helped improve the paper.

APPENDIX

Integral Constraints

a. Integral constraints in the continuous equations

Two integral constraints found in the continuous system of equations were used to guide the formulation of the vertical differencing scheme. The first is a constraint on the horizontal pressure-gradient force—that it not affect the vertically integrated momentum circulation in the absence of topography—and the second is the conservation of total energy under adiabatic, frictionless conditions. Detailed analyses of these constraints in a generalized vertical coordinate have been formulated for both hydrostatic atmospheres (e.g., Kasahara 1974; Arakawa and Konor 1996) and nonhydrostatic atmospheres (e.g., Staniforth and Wood 2008).

1) CONSTRAINT I: CONSTRAINT ON THE VERTICALLY INTEGRATED HORIZONTAL PRESSURE-GRADIENT FORCE

The contribution of the horizontal pressure-gradient force to the tendency of the vertically integrated horizontal momentum can be expressed as

$$\int_{\eta_S}^{\eta_T} m(\mathbf{HPGF})\, d\eta = -\nabla \int_{\eta_S}^{\eta_T} \left(\frac{p}{g}\frac{\partial \phi}{\partial \eta}\right) d\eta - p_S \nabla z_S, \quad \text{(A.1)}$$

where $\phi \equiv gz$ is the geopotential and z_T, η_T, and η_S are assumed constant. When the line integral of the

tangential component of (A.1) is taken along any closed curve, the first term on the rhs has a zero contribution because it is a gradient vector. The only contribution to the vertically integrated circulation of momentum comes from the last term, which is called the mountain torque term. When the closed curve is a contour of the surface topography, it is zero.

2) CONSTRAINT II: CONSERVATION OF TOTAL ENERGY

In the absence of diabatic heating and friction, the total energy of a fluid system is constant. Here, total energy is defined as the sum of the kinetic, geopotential, and internal energies. Conversions between these forms of energy take place at rates given by "conversion" terms that appear in the energy tendency equations. Total energy conservation is maintained through the cancellation of these conversion terms when deriving the total energy tendency equation.

(i) Kinetic energy equation

The tendency of kinetic energy can be expressed in flux form as

$$\frac{\partial}{\partial t}(mK) + \nabla \cdot (m\mathbf{v}K) + \frac{\partial}{\partial \eta}(m\dot{\eta}K) = m\mathbf{v} \cdot (\mathbf{HPGF}) + mw\,(\mathrm{VPGF}) - mwg$$
$$= -m\alpha\omega - \frac{\partial}{\partial \eta}\left(\frac{p}{g}\frac{\partial \phi}{\partial t}\right) + \frac{\partial}{\partial t}\left(\frac{p}{g}\frac{\partial \phi}{\partial \eta}\right) - mwg, \tag{A.2}$$

where $K = \frac{1}{2}(\mathbf{v} \cdot \mathbf{v} + w^2)$ is the kinetic energy per unit mass, α is the specific volume, $\omega \equiv Dp/Dt$, and friction is neglected. This equation is obtained by taking the dot product of $m\mathbf{v}$ and (2.5), and adding mw times (2.9), and combining with (2.2), (2.3), (2.6a), and (2.10a). Note that $m\alpha\omega$ is the conversion term between the thermodynamic and kinetic energy, and mwg is the conversion term between the kinetic and geopotential energy.

(ii) Internal energy equation

For frictionless atmospheric processes, the first law of thermodynamics can be expressed as

$$\frac{\partial}{\partial t}(mc_vT) + \nabla \cdot (m\mathbf{v}c_vT) + \frac{\partial}{\partial \eta}(m\dot{\eta}c_vT) = m\alpha\omega + mQ - \frac{\partial}{\partial t}\left(\frac{p}{g}\frac{\partial \phi}{\partial \eta}\right) - \nabla \cdot \left(\frac{p}{g}\frac{\partial \phi}{\partial \eta}\mathbf{v}\right) - \frac{\partial}{\partial \eta}\left(\frac{p}{g}\frac{\partial \phi}{\partial \eta}\dot{\eta}\right), \tag{A.3}$$

where c_vT is the internal energy. This equation is obtained by combining (2.2), (2.8), (2.12), and (2.14). Note that the first term on the rhs is the conversion term between the thermodynamic and kinetic energy, which appears with the opposite sign to that in (A.2). Equation (A.3) can be rewritten in terms of enthalpy, defined as $h \equiv c_vT + p\alpha$, for which $dh = c_pdT$. The result is

$$\frac{\partial}{\partial t}(mc_pT) + \nabla \cdot (m\mathbf{v}c_pT) + \frac{\partial}{\partial \eta}(m\dot{\eta}c_pT) = m\alpha\omega + mQ. \tag{A.4}$$

(iii) Geopotential energy equation

Multiplying (2.13) by mg and using the continuity Eq. (2.2), the geopotential energy equation can be written as

$$\frac{\partial}{\partial t}(m\phi) + \nabla \cdot (m\mathbf{v}\phi) + \frac{\partial}{\partial \eta}(m\dot{\eta}\phi) = mwg. \tag{A.5}$$

Note the energy conversion term mwg appears with the opposite sign to that in the kinetic energy Eq. (A.2).

(iv) Total energy equation

The total energy equation is obtained by adding (A.2), (A.3), and (A.5), and canceling the energy conversion terms, to obtain

$$\frac{\partial}{\partial t}(mE) + \nabla \cdot (m\mathbf{v}E) + \frac{\partial}{\partial \eta}(m\dot{\eta}E)$$
$$= mQ - \nabla \cdot \left(\frac{p}{g}\frac{\partial \phi}{\partial \eta}\mathbf{v}\right) - \frac{\partial}{\partial \eta}\left[\frac{p}{g}\left(\frac{\partial \phi}{\partial t} + \dot{\eta}\frac{\partial \phi}{\partial \eta}\right)\right], \tag{A.6}$$

where $E \equiv c_vT + K + \phi$ is the total energy. The last two terms on the rhs are flux divergence terms that represent the spatial redistribution of energy. When integrated over the domain, they make no contribution to the total energy budget except for contributions from the boundaries. Therefore, total energy is globally conserved for adiabatic, frictionless processes.

b. Vertically discrete continuity equation for mass at layer edges

Arakawa and Konor (1996) derived a flux-form continuity equation written in terms of the layer-edge pseudodensity to facilitate the development of conservation properties for layer-edge quantities. Our vertical-differencing scheme uses the same method, which is reviewed here. The relations are used in the discrete integral constraint analysis to follow. The layer-edge continuity equation is

$$\frac{\partial m_{k+1/2}}{\partial t} + \nabla \cdot (m\mathbf{v})_{k+1/2} + \frac{(m\dot{\eta})_{k+1} - (m\dot{\eta})_k}{(\delta\eta)_{k+1/2}} = 0 \quad \text{for } k = 1, 2, \cdots, K-1, \tag{A.7}$$

$$\frac{\partial m_{1/2}}{\partial t} + \nabla \cdot (m\mathbf{v})_{1/2} + \frac{(m\dot{\eta})_1}{(\delta\eta)_{1/2}} = 0, \tag{A.8}$$

and

$$\frac{\partial m_{K+1/2}}{\partial t} + \nabla \cdot (m\mathbf{v})_{K+1/2} - \frac{(m\dot{\eta})_K}{(\delta\eta)_{K+1/2}} = 0, \tag{A.9}$$

where the layer-edge masses are

$$m_{k+1/2} \equiv \frac{1}{2}\frac{(\delta\eta)_k m_k + (\delta\eta)_{k+1} m_{k+1}}{(\delta\eta)_{k+1/2}} \quad \text{for } k = 1, 2, \cdots, K-1, \tag{A.10}$$

and

$$m_{1/2} \equiv m_1, \quad m_{K+1/2} \equiv m_K. \tag{A.11}$$

The horizontal mass flux interpolated to layer edges is

$$(m\mathbf{v})_{k+1/2} \equiv \frac{1}{2}\frac{(\delta\eta)_k (m\mathbf{v})_k + (\delta\eta)_{k+1}(m\mathbf{v})_{k+1}}{(\delta\eta)_{k+1/2}} \quad \text{for } k = 1, 2, \cdots, K-1, \tag{A.12}$$

and

$$(m\mathbf{v})_{1/2} \equiv (m\mathbf{v})_1, \quad (m\mathbf{v})_{K+1/2} \equiv (m\mathbf{v})_K. \tag{A.13}$$

The layer-center vertical mass fluxes are

$$(m\dot{\eta})_k \equiv \frac{1}{2}[(m\dot{\eta})_{k+1/2} + (m\dot{\eta})_{k-1/2}] \quad \text{for } k = 2, 3, \cdots, K-1, \tag{A.14}$$

and

$$(m\dot{\eta})_1 \equiv \frac{1}{2}(m\dot{\eta})_{1/2}, \quad (m\dot{\eta})_K \equiv \frac{1}{2}(m\dot{\eta})_{K-1/2}. \tag{A.15}$$

Finally, the generalized layer-edge thicknesses are

$$(\delta\eta)_{k+1/2} \equiv \frac{1}{2}[(\delta\eta)_k + (\delta\eta)_{k+1}] \quad \text{for } k = 1, 2, \cdots, K-1, \tag{A.16}$$

and

$$(\delta\eta)_{1/2} \equiv \frac{1}{2}(\delta\eta)_1, \quad (\delta\eta)_{K+1/2} \equiv \frac{1}{2}(\delta\eta)_K. \tag{A.17}$$

As in Arakawa and Konor (1996), it can be shown that the vertical sum of the layer-center continuity Eq. (3.1) times $(\delta\eta)_k$ is equivalent to the vertical sum of the layer-edge continuity Eqs. (A.7)–(A.9) times $(\delta\eta)_{k+1/2}$.

c. Integral constraints in the vertically discrete equations for $\eta = z$

Here, we demonstrate that integral constraints I and II are satisfied by the discrete governing equations of section 3 for the case of z coordinates, that is, for $\eta = z$, but not for the general case. A scheme that satisfies these integral constraints for the generalized coordinate η was developed in Toy (2008). However, the scheme supports a vertical computational mode in the potential temperature field, so it is not used in the model. Based on the potential harmful effects of this computational mode on atmospheric simulations, as shown in Arakawa and Moorthi (1988) and Arakawa and Konor (1996), we believe that the benefit of avoiding this computational mode outweighs that of formally satisfying constraints I and II.

1) CONSTRAINT I: CONSTRAINT ON THE VERTICALLY INTEGRATED HORIZONTAL PRESSURE-GRADIENT FORCE

In z coordinates, $\nabla\phi$ equals zero; therefore, the HPGF given by (3.6) becomes

$$(\mathbf{HPGF})_k = -\tilde{\theta}_k \nabla \Pi_k \quad \text{for } k = 1, 2, \cdots, K. \tag{A.18}$$

Using (3.19)–(3.22) in (A.18), the layer mass-weighted HPGF can be written as

$$[m(\mathbf{HPGF})]_k (\delta\eta)_k = -\nabla\left[\frac{p_k}{g}(\phi_{k+1/2} - \phi_{k-1/2})\right]. \tag{A.19}$$

Since the rhs of (A.19) is a gradient term, it generates zero circulation of momentum when integrated about a closed curve and, therefore, constraint I is satisfied.

2) CONSTRAINT II: CONSERVATION OF TOTAL ENERGY

For $\eta = z$, the vertical difference scheme conserves the globally integrated total energy through the consistency of the energy conversion terms derived from the discrete governing equations. To show this, we begin by taking the dot product of $(m\mathbf{v}\delta\eta)_k$ and (A.18), adding $(mw\delta\eta)_{k+1/2}$ times (3.3), and summing in the vertical. The result is the work done by the pressure-gradient forces given by

$$\sum_{k=1}^{K}[m\mathbf{v}\cdot(\mathbf{HGPF})]_k(\delta\eta)_k+\sum_{k=0}^{K-1}[mw\cdot(\mathrm{VGPF})]_{k+1/2}(\delta\eta)_{k+1/2}$$
$$=-\sum_{k=1}^{K}m_k\alpha_k\left(\frac{\partial p_k}{\partial t}+\mathbf{v}_k\cdot\nabla p_k\right)(\delta\eta)_k-\sum_{k=1}^{K-1}w_{k+1/2}m_{k+1/2}\theta_{k+1/2}(\Pi_{k+1}-\Pi_k)$$
$$+\sum_{k=1}^{K}\frac{\partial}{\partial t}\left[\frac{p_k}{g}(\phi_{k+1/2}-\phi_{k-1/2})\right], \tag{A.20}$$

where we used (A.16), (A.17), and (3.5) for $\eta = z$. Comparing (A.20) and (A.2), we can identify the column-integrated energy conversion term between thermodynamic and kinetic energy as

$$\sum_{k=1}^{K}(m\alpha\omega)_k(\delta\eta)_k=\sum_{k=1}^{K}m_k\alpha_k\left(\frac{\partial p_k}{\partial t}+\mathbf{v}_k\cdot\nabla p_k\right)(\delta\eta)_k+\sum_{k=1}^{K-1}w_{k+1/2}m_{k+1/2}\theta_{k+1/2}(\Pi_{k+1}-\Pi_k)\cdot \tag{A.21}$$

To derive the corresponding energy conversion term from the thermodynamic energy equation, we begin by multiplying (3.13)–(3.15) by $(m\Pi\delta\eta)_{k+1/2}$, and use (3.2), (A.11), (A.14), (A.15), (A.17), (3.9), (3.16), (3.17), and the fact that $\dot{\eta}_{k+1/2} = w_{k+1/2}$ in z coordinates to obtain

$$\sum_{k=1}^{K}m_k\Pi_k\left(\frac{\partial\tilde{\theta}_k}{\partial t}+\mathbf{v}_k\cdot\nabla\tilde{\theta}_k\right)(\delta\eta)_k-\sum_{k=1}^{K}\tilde{\theta}_K\Pi_k[(m\dot{\eta})_{k+1/2}-(m\dot{\eta})_{k-1/2}]-\sum_{k=1}^{K-1}w_{k+1/2}m_{k+1/2}\theta_{k+1/2}(\Pi_{k+1}-\Pi_k)$$
$$=\sum_{k=0}^{K}(mQ)_{k+1/2}(\delta\eta)_{k+1/2}. \tag{A.22}$$

Finally, applying (3.1), (3.2), and (3.20)–(3.22) in (A.22), we obtain

$$\sum_{k=1}^{K}\frac{\partial}{\partial t}(mc_pT)_k(\delta\eta)_k+\sum_{k=1}^{K}\nabla\cdot(m\mathbf{v}c_pT)_k(\delta\eta)_k=\sum_{k=1}^{K}m_k\alpha_k\left(\frac{\partial p_k}{\partial t}+\mathbf{v}_k\cdot\nabla p_k\right)(\delta\eta)_k$$
$$+\sum_{k=1}^{K-1}w_{k+1/2}m_{k+1/2}\theta_{k+1/2}(\Pi_{k+1}-\Pi_k)+\sum_{k=0}^{K}(mQ)_{k+1/2}(\delta\eta)_{k+1/2}. \tag{A.23}$$

Comparing (A.23) to (A.4), the first two terms on the rhs of (A.23) correspond to the energy conversion term $m\alpha\omega$, which is identical to (A.21); therefore, the energy conversion between the thermodynamic and kinetic energies is conservative.

The last step in determining the total energy conservation by the vertically discrete system of governing equations is to check the consistency of the energy conversion term between the kinetic and geopotential energies derived from the vertical momentum and geopotential tendency equations. Multiplying $(mw)_{k+1/2}$ by the vertical momentum equation, given by the discrete form of (2.9) evaluated at layer edges, the energy conversion term is $-g(mw)_{k+1/2}$. To derive the geopotential energy equation, we multiply (3.10) and (3.18) by $m_{k+1/2}$ and add $\phi_{k+1/2}$ times the layer-edge continuity Eqs. (A.7)–(A.9) to obtain

$$\frac{\partial}{\partial t}(m\phi)_{k+1/2} + \nabla\cdot(m\mathbf{v}\phi)_{k+1/2} + \frac{(\widetilde{m\dot{\eta}\phi})_{k+1} - (\widetilde{m\dot{\eta}\phi})_k}{(\delta\eta)_{k+1/2}} = g(mw)_{k+1/2} \quad \text{for } k = 1, 2, \cdots, K-1, \tag{A.24}$$

$$\frac{\partial}{\partial t}(m\phi)_{1/2} + \nabla\cdot(m\mathbf{v}\phi)_{1/2} + \frac{(\widetilde{m\dot{\eta}\phi})_1}{(\delta\eta)_{1/2}} = g(mw)_{1/2}, \tag{A.25}$$

and

$$\frac{\partial}{\partial t}(m\phi)_{K+1/2} + \nabla\cdot(m\mathbf{v}\phi)_{K+1/2} - \frac{(\widetilde{m\dot{\eta}\phi})_K}{(\delta\eta)_{K+1/2}} = g(mw)_{K+1/2}, \tag{A.26}$$

where the vertical flux of the geopotential energy at layer centers is defined as

$$(\widetilde{m\dot{\eta}\phi})_k \equiv \frac{1}{2}[(m\dot{\eta})_{k-1/2}\phi_{k+1/2} + (m\dot{\eta})_{k+1/2}\phi_{k-1/2}] \quad \text{for } k = 1, 2, \cdots, K. \tag{A.27}$$

In (A.27), we note that the geopotential flux terms involve products of the mass flux and geopotential at different levels. Equations (A.24)–(A.26) are in flux form, so geopotential energy is conserved under vertical advection, and the energy conversion term $g(mw)_{k+1/2}$ appears in the same form but of opposite sign as that derived above; therefore, the requirements for total energy conservation are met.

REFERENCES

Andrews, D. G., 1983: A finite-amplitude Eliassen–Palm theorem in isentropic coordinates. *J. Atmos. Sci.,* **40,** 1877–1883.

Arakawa, A., and S. Moorthi, 1988: Baroclinic instability in vertically discrete systems. *J. Atmos. Sci.,* **45,** 1688–1707.

——, and C. S. Konor, 1996: Vertical differencing of the primitive equations based on the Charney–Phillips grid in hybrid σ–θ vertical coordinates. *Mon. Wea. Rev.,* **124,** 511–528.

Benjamin, S. G., G. A. Grell, J. M. Brown, and T. G. Smirnova, 2004: Mesoscale weather prediction with the RUC hybrid isentropic–terrain-following coordinate model. *Mon. Wea. Rev.,* **132,** 473–494.

Bleck, R., 1984: An isentropic coordinate model suitable for lee cyclogenesis simulation. *Riv. Meteor. Aeronaut.,* **43,** 189–194.

——, and S. Benjamin, 1993: Regional weather prediction with a model combining terrain-following and isentropic coordinates. Part I: Model description. *Mon. Wea. Rev.,* **121,** 1770–1785.

Charney, J. G., and N. A. Phillips, 1953: Numerical integration of the quasi-geostrophic equations for barotropic and simple baroclinic flows. *J. Meteor.,* **10,** 71–99.

Davies, T., M. J. P. Cullen, A. J. Malcolm, M. H. Mawson, A. Staniforth, A. A. White, and N. Wood, 2005: A new dynamical core for the Met Office's global and regional modelling of the atmosphere. *Quart. J. Roy. Meteor. Soc.,* **131,** 1759–1782.

Dietachmayer, G. S., and K. K. Droegemeier, 1992: Application of continuous dynamic grid adaption techniques to meteorological modeling. Part I: Basic formulation and accuracy. *Mon. Wea. Rev.,* **120,** 1675–1706.

Dowling, T. E., and Coauthors, 2006: The EPIC atmospheric model with an isentropic/terrain-following hybrid vertical coordinate. *Icarus,* **182,** 259–273.

Doyle, J. D., and Coauthors, 2000: An intercomparison of model-predicted wave breaking for the 11 January 1972 Boulder windstorm. *Mon. Wea. Rev.,* **128,** 901–914.

Durran, D. R., and J. B. Klemp, 1983: A compressible model for the simulation of moist mountain waves. *Mon. Wea. Rev.,* **111,** 2341–2361.

Eliassen, A., and E. Palm, 1961: On the transfer of energy in stationary mountain waves. *Geofys. Publ.,* **22** (3), 1–23.

——, and E. Raustein, 1968: A numerical integration experiment with a model atmosphere based on isentropic coordinates. *Meteor. Ann.,* **5** (2), 45–63.

Gal-Chen, T., and R. C. J. Somerville, 1975: On the use of a coordinate transformation for the solution of the Navier–Stokes equations. *J. Comput. Phys.,* **17,** 209–228.

He, Z., 2002: A non-hydrostatic model with a generalized vertical coordinate. Ph.D. thesis, University of Miami, 99 pp.

Hirt, C. W., A. A. Amsden, and J. L. Cook, 1974: An arbitrary Lagrangian–Eulerian computing method for all flow speeds. *J. Comput. Phys.,* **14,** 227–253.

Hsu, Y.-J. G., and A. Arakawa, 1990: Numerical modeling of the atmosphere with an isentropic vertical coordinate. *Mon. Wea. Rev.,* **118,** 1933–1959.

Johnson, D. R., T. H. Zapotocny, F. M. Reames, B. J. Wolf, and R. B. Pierce, 1993: A comparison of simulated precipitation by hybrid isentropic-sigma and sigma models. *Mon. Wea. Rev.,* **121,** 2088–2114.

Kasahara, A., 1974: Various vertical coordinate systems used for numerical weather prediction. *Mon. Wea. Rev.,* **102,** 509–522.

Klemp, J. B., and D. K. Lilly, 1978: Numerical simulation of hydrostatic mountain waves. *J. Atmos. Sci.,* **35,** 78–107.

Konor, C. S., and A. Arakawa, 1997: Design of an atmospheric model based on a generalized vertical coordinate. *Mon. Wea. Rev.,* **125,** 1649–1673.

Laprise, R., 1992: The Euler equations of motion with hydrostatic pressure as an independent variable. *Mon. Wea. Rev.,* **120,** 197–207.

Lilly, D. K., and E. J. Zipser, 1972: The front range windstorm of 11 January 1972—A meteorological narrative. *Weatherwise,* **25** (2), 56–63.

Lin, S.-J., 2004: A ''vertically Lagrangian'' finite-volume dynamical core for global models. *Mon. Wea. Rev.,* **132,** 2293–2307.

Lorenz, E. N., 1960: Energy and numerical weather prediction. *Tellus,* **12,** 364–373.

Peltier, W. R., and T. L. Clark, 1979: The evolution and stability of finite-amplitude mountain waves. Part II: Surface wave drag and severe downslope windstorms. *J. Atmos. Sci.,* **36,** 1498–1529.

Queney, P., 1948: The problem of airflow over mountains: A summary of theoretical studies. *Bull. Amer. Meteor. Soc.,* **29,** 16–26.

Satoh, M., T. Matsuno, H. Tomita, H. Miura, T. Nasuno, and S. Iga, 2008: Nonhydrostatic Icosahedral Atmospheric Model (NICAM) for global cloud resolving simulations. *J. Comput. Phys.,* **227,** 3486–3514.

Schaack, T. K., T. H. Zapotocny, A. J. Lensen, and D. R. Johnson, 2004: Global climate simulation with the University of Wisconsin global hybrid isentropic coordinate model. *J. Climate,* **17,** 2998–3016.

Skamarock, W. C., 1998: A hybrid-coordinate nonhydrostatic model. Preprints, *12th Conf. on Numerical Weather Prediction,* Phoenix, AZ, Amer. Meteor. Soc., 232–235.

——, J. B. Klemp, J. Dudhia, D. O. Gill, D. M. Barker, W. Wang, and J. G. Powers, 2005: A description of the Advanced Research WRF version 2. NCAR Tech. Note TN-468+STR, 88 pp.

Smagorinsky, J., 1963: General circulation experiments with the primitive equations. I: The basic experiment. *Mon. Wea. Rev.,* **91,** 99–164.

Smith, R. B., 1979: The influence of mountains on the atmosphere. *Advances in Geophysics,* Vol. 21, Academic Press, 87–230.

Staniforth, A., and N. Wood, 2008: Aspects of the dynamical core of a nonhydrostatic, deep-atmosphere, unified weather and climate-prediction model. *J. Comput. Phys.,* **227,** 3445–3464.

Starr, V. P., 1945: A quasi-Lagrangian system of hydrodynamical equations. *J. Meteor.,* **2,** 227–237.

Takacs, L. L., 1985: A two-step scheme for the advection equation with minimized dissipation and dispersion errors. *Mon. Wea. Rev.,* **113,** 1050–1065.

Thuburn, J., and T. J. Woollings, 2005: Vertical discretizations for compressible Euler equation atmospheric models giving optimal representation of normal modes. *J. Comput. Phys.,* **203,** 386–404.

Toy, M. D., 2008: Design of a nonhydrostatic atmospheric model based on a generalized vertical coordinate. Ph.D. dissertation, Colorado State University, 231 pp.

——, and D. A. Randall, 2007: Comment on the article ''Vertical discretizations for compressible Euler equation atmospheric models giving optimal representation of normal modes'' by Thuburn and Woollings. *J. Comput. Phys.,* **223,** 82–88.

Uccellini, L. W., D. R. Johnson, and R. E. Schlesinger, 1979: An isentropic and sigma coordinate hybrid numerical model: Model development and some initial tests. *J. Atmos. Sci.,* **36,** 390–414.

Zängl, G., 2007: An adaptive vertical coordinate formulation for a nonhydrostatic model with flux-form equations. *Mon. Wea. Rev.,* **135,** 228–239.

Zhu, Z., J. Thuburn, B. J. Hoskins, and P. H. Haynes, 1992: A vertical finite-difference scheme based on a hybrid σ–θ–p coordinate. *Mon. Wea. Rev.,* **120,** 851–862.